Antimony Oxide Glasses and Their Nanocomposites for Optical, Photonic and Nanophotonic Applications

Tirtha Som and Basudeb Karmakar*

Glass Science and Technology Section, Glass Division,
Central Glass and Ceramic Research Institute
Council of Scientific and Industrial Research (CSIR, India),
196, Raja S. C. Mullick Road, Kolkata 700 032, India

1. Introduction

Contemporary glass research focuses on the development of specialized or unusual glasses as a novel media for photonic, plasmonic and nanophotonic technologies by incorporating luminescent rare-earth ions, metal nanoparticles, semiconductor nanoparticles, etc and their hybrids [1-3]. Research in these fast emerging areas require development of new glass compositions and in this respect, unlike the conventional silicate, borate and phosphate glasses, heavy metal oxide glasses like bismuth, tellurite, lead, and/or antimony acting as glass structure network formers is expected to play a dramatic role as they possess some exciting properties like high refractive index, large transmission window, large non-linear optical properties, low phonon energy and high dielectric constant.

There has been considerable investigation on Bi-, Te- and Pb- glasses but Sb-based glasses remain widely unexploited [4]. Antimony(III) oxide (Sb_2O_3) has mainly been used as refining or fining agent for glass melts. Glass forming ability of $Sb_2O_3$was first predicted by Zachariasen [5] in 1932 but it was 1939 when Kordes first succeeded to prepare a few milligrams of antimony glass overcoming the problems of preparation [6]. Since then very few authors have investigated this glass and very few measured properties have been published [7-14]. To the best of knowledge there is no report of preparation of monolithic (bulk) antimony oxide glasses containing more than 50 mol% of Sb_2O3. Literature reports show that they are obtained in pulverized forms. This because Sb3+ cation has weak field strength (0.73), Sb_2O_3 has high volatization rate and antimony glasses have very high tendencies to crystallize [4].

We have developed new monolithic Sb_2O_3 based glasses and for the first time we could incorporate in antimony glass the trivalent RE ions and metallic nanoparticles separately and as hybrids. We have studied their optical and other properties [15-22] for

applications in photonics and nanotechnology. This chapter presents some very interesting results of our recent basic research and new aspects of Sb_2O_3 glasses.

2. Experimental

2.1 Preparation of the glasses and nanocomposites

The raw materials were antimony(III) oxide, Sb_2O_3 (GR, 99%, Loba Chemie) and potassium metaborate, $KBO_2.xH_2O$ (15.7% H_2O, Johnson Matthey). 20 g of glasses were prepared by melting the well mixed batches of calculated composition in a high purity silica crucible at 900^oC for 10 min with intermittent stirring for 30 sec in air in a raising hearth electric furnace. All the molten samples were cast into carbon plates in air and annealed at 260ºC for 3h to remove thermal stresses followed by slow cooling (1ºC/ min) down to room temperature.

For synthesis of RE^{3+} doped glasses and nano-metal doped glasses, the required quantities of europium(III) oxide, Eu_2O_3 (99.9%, Alfa Aesar), Samarium(III) oxide, Sm_2O_3 (99.99 % Indian Rare Erath), erbium(III) oxide, Er_2O_3 (99.99%, Laborat), and gold(III) chloride, $HAuCl_4.xH_2O$, (49 % Au, Loba Chemie) were added in excess to the mother (base) glass batch and melted similarly.

2.2 Characterization of the glasses and nanocomposites and measurements of properties

The bulk densities (error ± 0.8 %) of the samples were measured by Archimedes method using toluene (a non-polar hydrophobic solvent) as immersion liquid because water may have some corrosive effect dissolving the antimony glasses to some extent. The refractive indices and other theoretically predicted respective glass properties were determined using SciGlass (Glass Properties Information System, Version 6.7) software following the Priven-2000 method. The softening point (T_s) (accuracy $\pm$2 ^oC) of were measured by a glass softening point system (Harrop/Labino, Model SP-3A). The coefficient of thermal expansion (CTE, α in the temperature range 50-150ºC), glass transition temperature (T_g) and deformation temperature (T_d) were measured using a horizontal vitreous silica dilatometer (DIL 402C, Netzch-Gerätebau GmbH, Bavaria, Germany) with heating rate 5 K/min. These values were reproducible with ±1ºC for all samples. Dielectric constant (accuracy $\pm$ 0.7%) was measured at room temperature using a LCR meter (Hioki 3532-50 LCR HiTESTER, Japan) at 1 MHz frequency by probe method after coating opposite sides of square shaped polished samples

(cross-sectional area of 10×10 mm^2 and thickness 2 mm) with a thin layer of conducting silver paint and dried at 140 °C to serve as electrodes.

The infrared transmission spectra (FT-IRTS) were measured by Fourier transform infrared spectrometer (FTIR 1615, Perkin-Elmer Corporation, Norwalk, USA) (resolution ± 2 cm^{-1}) and for infrared reflection spectra measurements a specular reflectance attachment accessory was attached with the FTIR instrument at an incident angle of 15º. The UV-Vis absorption/ transmission spectra (accuracy ± 0.1 nm) were obtained with a double-beam spectrophotometer (Lambda 20, Perkin-Elmer Corporation, Norwalk, USA). The fluorescence spectra (accuracy ± 0.2 nm) were measured with a Spex, Fluorolog 2 fluorescence spectrophotometer (New Jersey, United States) with 150 W Xenon lamp as excitation source and a photomultiplier tube as a detector. The excitation slit (1.25 mm) and emission slit (0.5 mm) were kept same for all samples. The X-ray diffraction patterns of the bulk samples were recorded in an X'pert Pro MPD diffractometer (PANalytical, Almelo, The Netherlands) using Ni-filtered Cukα radiation with step size 0.05º (2θ) step time 0.5 sec, from 10 to 80º.

Field emission scanning electron microscopy (FESEM) images of the fracture surfaces of glasses and nanocomposites were taken with Gemini Zeiss Supra™ 35VP model (Carl Zeiss Microimaging GmbH, Berlin, Germany) after etching the samples in 5 vol% HNO_3 for 1 min. TEM was done using a Jeol (JEM 2010) operating at an accelerating voltage of 200 kV. Sample for TEM were prepared by ultrasonication (dispersion) of finely powdered nanocomposite samples in acetone, placing a drop of the supernatant dispersion on a carbon coated copper grid and drying under IR lamp at room temperature. The SAED images have been taken by focusing the electron beam on the metal nanoparticles.

3. Results and discussion

3.1 Low Phonon Monolithic K_2O-B_2O_3-Sb_2O_3 (KBS) Glasses: Structure and Properties

Composition and some physical properties of the samples are indicated in Table 1. The samples having higher Sb_2O_3 content are yellow in color due to host absorption caused by the transition between HOMO (Sb 5s + O 2pπ) and LUMO (Sb 5p) [11].

Table 1. Nominal composition and some properties of the KBS smaples

Sample No.	Composition (mol %)			Color	Form (Nature)
	K_2O	B_2O_3	Sb_2O_3		
B1	5	5	90	Deep yellow	Translucent large broken pieces (devitrified)
B2	10	10	80	Yellow	Transparent monolith (glass)
B3	15	15	70	Yellow	Transparent monolith (glass)
B4	20	20	60	Pale -yellow	Transparent vmonolith (devitrified)
B5	25	25	50	Colorless	Transparent monolith (devitrified)
B6	30	30	40	Colorless	Transparent monolith but surface easily attacked by moisture (devitrified)
B7	35	35	30	White	Opaque small broken pieces (devitrified)

The X-ray diffraction patterns of the samples in comparison to the raw material Sb_2O_3 used in batch are shown in Fig. 1. Antimony oxides, in general, are known to exist in a wide range of compositions and display interconvertable polymorphism. The two common forms are senarmontite (cubic) and valentinite (orthorhombic) consisting of Sb_4O_6 molecules and chains of SbO_3 trigonal pyramids respectively [23,24]. The polymorphic forms of Sb_2O_4 are the orthorhombic α-phase (cervantite) and there is also high temperature monoclinic β-phase [23,24]. The XRD patterns indicate that when the natural when the natural and conditional glass former (B_2O_3 and Sb_2O_3 respectively) are present in near-equal amounts, crystallization sets in and devitrified monoliths are obtained. This is probably due to the large difference in field strengths of Sb^{3+} (F = 0.73), B^{3+} (F = 1.34) and alkali K^+ (F =0.13) ions [4].

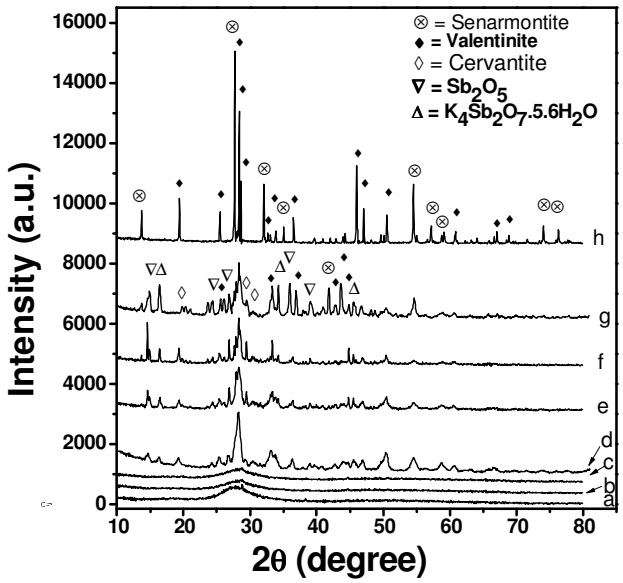

Fig. 1. X-ray diffractograms of samples (a) B1, (b) B2, (c) B3, (d) B4, (e) B5, (f) B6, (g) B7 (for composition see Table 1) and (h) Sb_2O_3 used as starting material is shown for comparison.

The XRD results clearly support valentinite as the dominant phase with small amount of senarmontite, cervantite and potassium antimony hydroxide. Orthorhombic Sb_2O_3 is known to crystallize in the space group Pccn (D_{2h}^{10}) and is built up of infinite polymeric Sb-O-Sb chains running along the *c* axis with Sb-O distances of 20 Å. As a result we get some amazing microstructures which are usually not observed in other heavy metal oxide glasses. Their FESEM images of devitrified glasses B4-B6 depict gradual change of microstructures from granule clustered to cell-wall-like to house-of-disks respectively which consists mainly of nanocrystallites of valentinite Sb_2O_3 and have been left after elimination of borate-rich phase by acid.

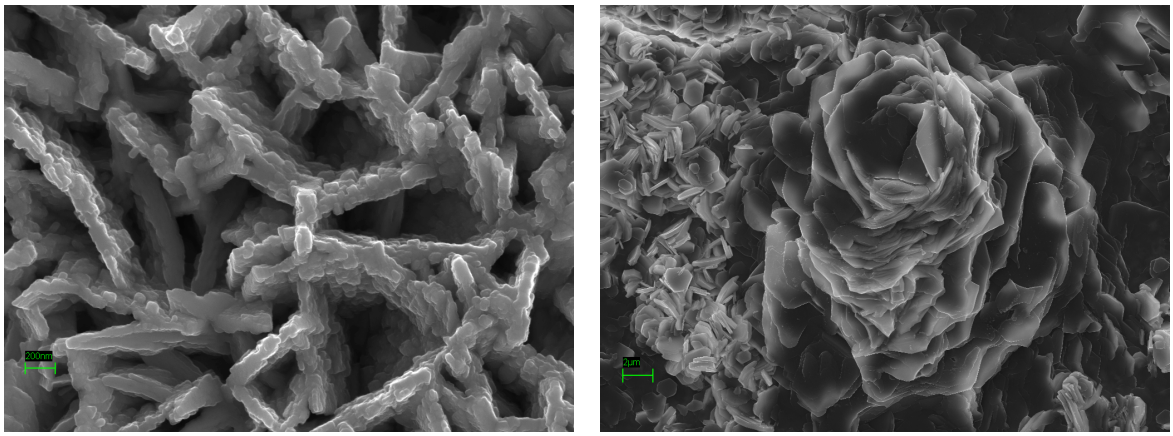

Fig. 2. Representative FESEM images of antimony oxide glasses (a) B4 (scale 200 nm) showing cell-wall like microstructure and (b) B6 (scale 2 μm) showing disk-like microstructures which accumulates to develop rose-flower-like microstructure.

Structural investigation using the Fourier Transform IR transmission (FT-IRTS) spectra (KBr pellet method), particularly in the fingerprint region (400-1500 cm^{-1}) in comparison with those of raw materials (Fig. 3), provide information about structure (short range order) of antimony oxide glasses. The bands located at 692, 592, 546 and 492 cm^{-1} corresponds to symmetric stretching, asymmetric stretching, symmetric bending and asymmetric bending Sb-O-Sb vibrations of valentinite form of SbO_3 trigonal pyramids with C_s or C_2 symmetry, respectively [9,11,24] thereby emphasizing the closeness of the glass structure to valentinite [9,11,24]. The small peak at 954 cm^{-1} is due to Sb-O stretching vibrations of senarmontite form of SbO_3 [9,11]. It may also be due to coincides with Si-O

stretching vibrations of SiO_4 tetrahedra which were contaminated from silica crucibles during the melting process [9]. This was also found by energy dispersive X-ray (EDX) spectra of the glasses. The contamination of small amount of silica is expected to aid in glass formation. The peak at 1231 cm^{-1} arises due to B-O stretching vibrations of $(BO_3)^{3-}$ unit in metaborate chains [25,26]. The region between 1000-1200 cm^{-1} and 1200-1500 cm^{-1} is generally attributed to asymmetric stretching vibrations of the B-O-B bond of tetragonal $[BO_4]$ and trigonal $[BO_3]$ unit respectively. The FT-IRTS spectra also support intense crystallization with decreasing Sb_2O_3 content in the samples. The peak at 1630 cm^{-1} arises due to bending vibrations of O-H group of H_2O molecules. The broad band around 3392 cm^{-1} corresponds to the stretching vibration of O-H group. While the small peak at 3277 cm^{-1} is due to hydrogen bonded OH ($-O-H^{\delta+}\ldots O^{\delta-}-$) and the small peak at 3554 cm^{-1} corresponds to free O-H group to the glass network [27]. The presence of water in the form of hydroxyl groups in the glasses is thus suggested.

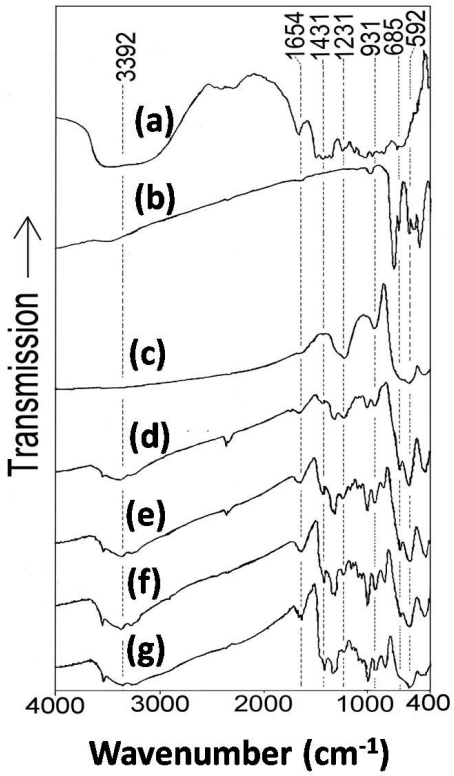

Fig. 3. Infrared transmission spectra (FT-IRTS) of (a) $KBO_2.xH_2O$, (b) Sb_2O_3, (c) B2, (d) B3, (e) B4, (f) B5 and (g) B6 (for composition see Table 1). Spectra of raw materials (a) and (b) are shown for comparison.

Thus antimony based glass structure resembles valentinite form of Sb_2O_3 having SbO_3 pyramids with the coordination number of Sb as 3. Oxygen atoms are present in three corners (Sb-O bond distance 2.0 Å) and the lone pairs of electrons of Sb^{3+} at the fourth corner [6]. The coordination polyhedra are joined by sharing corners to form double infinite chains with the lone pair pointing out from the chains. Such chains are held together by weak secondary Sb-O bonds with lengths greater than 2.6Å. The third oxygen in each SbO_3 unit takes part in Sb-O-B type bond formation [4,28]. The presence of common meta-centers and B-O-B vibrational bands in the IR spectra of the glasses supports the statement. Thus the structure essentially consists of long chains of entangled SbO_3 units. The introduction of the glass modifier K_2O probably breaks some linkages (B-O-B bonds, Sb-O-B bonds) and thereby the local symmetry of the glass network. This leads to the formation of non-bridging oxygen ions (NBOs) and introduction of dangling bonds (coordination defects).

During melting at high temperature (900ºC) small part of Sb^{3+} (in Sb_2O_3 used as the raw material) is expected to be converted to Sb^{5+} by accepting oxygen from air due to its multivalent characteristics according to the following reaction:

$$Sb_2O_3 + O_2 = Sb_2O_5 \qquad (1)$$

These Sb^{5+} ions enter into the glass as singly positive $[SbO_4]$ 4-coordinated units. The presence of positive $[SbO_4]$ would provide charge balance for the negative $[BO_4]$ units [9,11]. The existence of Sb_2O_5 crystals has been confirmed by XRD analysis. Earlier structural investigations of Sb_2O_3-B_2O_3 systems have shown that Sb5+ value reaches almost 15% of glasses containing 70 mol% Sb_2O_3 [13].

The phonon energy ($\hbar\omega$ or bond vibration energy of the building units) is an important glass property. The lower the phonon energy, the higher is the efficiency of unconversion of the doped RE^{3+} ions. The infrared reflection spectrum (IRRS) can to determine the phonon energy of glasses as alternation to Raman or phonon side band spctra. In IRRS, the main and the highest intensity band is assigned as the phonon energy which is established to be 602 cm^{-1} for Sb_2O_3 glasses (Fig. 4) and this value is very close to the theoretically predicted Sb-O-Sb stretching vibration of 605 cm^{-1}[24]. It is observed that the intensity of the 602 cm^{-1} band decreases with decrease of Sb_2O_3 content and the intensity of the 1207 cm^{-1} band increases indicating an increase in borate content. As a consequence, the IRRS curves show an isosbestic point at 777 cm^{-1} manifesting an existence of equilibrium between the two principle species, antimony and boron.

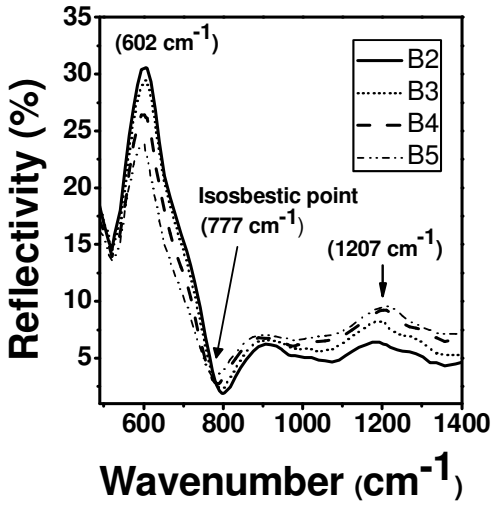

Fig. 4. Infrared reflection spectra (FT-IRRS) of monolithic antimony oxide glasses and devitrified glasses: B2, B3, B4 and B5 (for composition see Table 1).

Table 2 compares the relative phonon energies of various glasses with that of antimony glass. It is thus established that Sb_2O_3 glasses have low phonon energy analogous to that of fluoride glasses and are impending candidates for upconversion when doped with rare-earth (RE^{3+})-ions. We shall discuss the lasing properties of some RE^{3+} ions in antimony glass in the next sub-section and that they may be used as solid state laser materials in place of fluoride glass wherever suitable as they can be synthesized in ambient atmosphere, where as the fluoride glasses require sophisticated atmosphere controlled furnace.

Table 2. Comparison of phonon energies of various glasses

Glass	Phonon energies (cm^{-1})	References
Chalcogenide	200-300	[29]
Fluoride	500-600	[29]
Antimony oxide	600	Present study
Tellurite	600-850	[29]
Germanate	800-975	[29]
Silicate	1060-1150	[29]
Phosphate	1200-1350	[29]
Borate	1480-1340	[29]

Sb_2O_3 glasses have wide transmission window from ~393 nm (UV cut-off) to ~6700 nm (IR cut-off). The later is due to heavier atomic mass of Sb atom which contributes to the reduced strength or force constant of Sb-O bond by weak columbic interactions. Interestingly, the UV-Vis-NIR transmission spectra of KBS antimony glasses also yield isosbestic point at

393 nm (Fig. 5). This is because the position of the cutoff wavelength or fundamental absorption edge red-shifts towards higher wavelength by the increasing influence of non-bridging oxygen ions (NBOs) with increasing K_2O content [4]. While there is a decrease in transmittance of the glasses containing higher concentration of Sb_2O_3 due to high polarisability of Sb^{3+} cation with a lone pair of electrons and high polarization the O^{2-} anion which in turn increases the total electronic polarizability. A direct consequence is the molar refraction and refractive indices increases causing a greater loss of transmittance due to scattering.

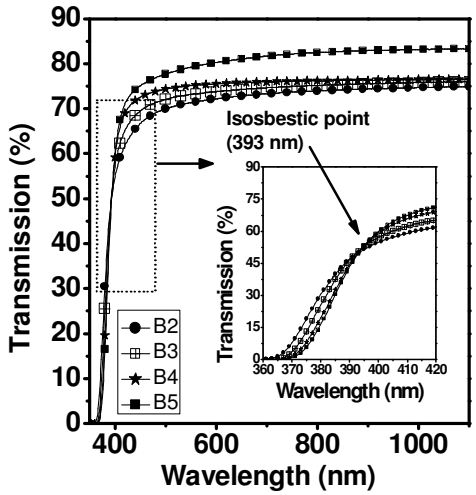

Fig. 5. UV-visible transmission spectra of the KBS samples (thickness: 1.0 mm, for composition see Table 1). Inset shows isosbestic point at 393 nm.

The band gap, E_{opt} (eV), of KBS glasses can be evaluated from the transmission spectra by plotting $(\alpha h\upsilon)^2$ vs. $h\upsilon$ [where absorption coefficient is $\alpha(\upsilon)$ in Tauc's plot], considering allowed direct transitions, and extrapolating the linear portion of the curve to intersect the photon energy ($h\upsilon$) axis at zero absorption [30]. The decrease in value of E_{opt} from 3.22 eV down to 3.15 eV with decreasing concentration of Sb_2O_3 understood in terms of structural changes in the glass system. In the present ternary system both Sb_2O_3 and B_2O_3 acts as network formers while K_2O as network modifier. The incorporation of K_2O increases the quantity of NBOs. Since NBOs are more easily excited than bridging oxygen, E_{opt} decreases with addition of K_2O and removal of Sb_2O_3. Thus these glasses are wide gap materials.

The KBS antimony glasses are found to possess high refractive index and dispersion (Table 3). They possess a very unique position in the legendary Abbe diagram of optical glasses (Fig. 6) and exhibit the potential of replacing the lead oxide (PbO) containing glasses with respect to environmental friendliness and low softening point.

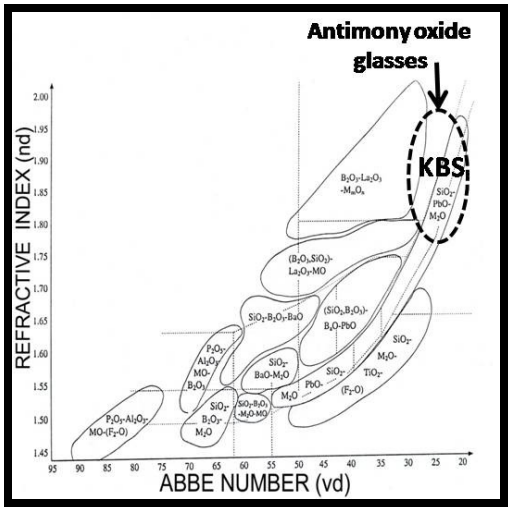

Fig. 6. Position of KBS antimony glasses in the legendary abbe diagram.

The experimental softening point (T_s), glass transition temperature (T_g), coefficient of thermal expansion (CTE), and dielectric constant (ε) of KBS glasses have been found to vary in the ranges 331-392ºC (± 2 °C), 234-264ºC (± 1 °C), 201-222 (± 1) $\times 10^{-7}$ K^{-1} and 12.4-14.5 (± 0.1) respectively (Table 3). The T_s and T_g are found to obey the empirical relation:

$$T_s = 3\ T_g / 2 \qquad (2)$$

Similar results have been reported for other Sb_2O_3 containing glasses [13]. These properties are found to be directly controlled by their fundamental property like covalent character and optical basicity of the glasses which are found to increase with increase in Sb_2O_3 content (Table 3).

Table 3. Some of experimental and calculated properties of the KBS antimony glasses and devitrified glasses

Property	Sample identity[a]/ Property value				
	B2	B3	B4	B5	B6
Measured Properties					
OH content (ppm), (± 0.4)	125	133	141	150	
Density ($g.cm^{-3}$), (± 0.04)	4.7650	4.5560	4.3467	4.0985	3.8658
Softening point (T_s, ± 2 ºC)	331	341	356	378	392
Glass transition temperature (T_g, ± 1) ºC)	234	246	255	259	264
Thermal expansion coefficient (CTE (± 1), $\alpha \times 10^{-7}$)	222	219	206	204	201
Dielectric constant (± 0.1)	14.5	14	13.3	13.2	12.4
Calculated Properties					
Covalent character, % (± 0.03)	48.55	46.50	44.49	42.50	40.55
Theoretical optical basicity, Λ_{th} (± 0.002)	1.072	1.035	0.994	0.950	0.901
Band gap (from UV-vis spectra)	3.22	3.19	3.17	3.15	-
Refractive index	2.001	1.948	1.892	1.835	1.775
Abbe number	23.12	23.86	24.80	26.01	27.65
Total molar polarizability, α_m ($Å^3$) (± 0.007)	10.40	9.60	8.77	7.97	7.10
Metallization criterion (M) (±0 .001)	0.4998	0.5178	0.5376	0.5590	0.5827

[a] For composition see Table 1

The extent of covalent bonding character may be calculated as [31]:

$$\text{Covalent character (\%)} = \exp[-0.25\,(\Delta\chi)^2] \times 100 \qquad (3)$$

where $\Delta\chi$ is the electronegativity of the composite, that is, the electronegativity difference ($\chi_A - \chi_C$) of the anions and the cations following the Pauling's scale [32]. It is found to vary in the range 48.55-40.55 % and decreased with decrease in Sb_2O_3 content.

The optical basicity, as proposed by Duffy and Ingram [33,34], is used as parameter to determine the acid-base properties of the glass in terms of the electron density carried by oxygen. It represents the average electron donation capacity of the oxide (II) species in the medium after the polarization of their electron charge clouds by constituent cations. The theoretical (ideal) optical basicity (Λ_{th}), is calculated as [33-35]:

$$\Lambda_{th} = X(Sb_2O_3)\,\Lambda(Sb_2O_3) + X(B_2O_3)\,\Lambda(B_2O_3) + X(K_2O)\,\Lambda(K_2O) \qquad (4)$$

where, $X(Sb_2O_3)$, $X(B_2O_3)$ and $X(K_2O)$ are the equivalent fractions based on the proportion of oxygen, each oxide contributes to the overall glass stoichiometry and $\Lambda(Sb_2O_3) = 1.18$, $\Lambda(B_2O_3) = 0.42$ and $\Lambda(K_2O) = 1.4$ are the basicities assigned to individual oxides [35].

Both Sb^{3+} and K^{+} have considerably less field strength (0.73 and 0.13 respectively) than B^{3+}(1.34) [4]. Consequently they play a major role of decreasing the T_s and T_g. Besides covalent bonds are less strong than ionic bonds and generally, the compounds with a more covalent bonds or covalent character posses lower softening points (T_s) and glass transition temperatures (T_g). However, one should also consider the influence of structural changes on these properties as well.

The CTE values are seen to increases with increase of Sb_2O_3 concentration. Generally the CTE increases as bond strength reduces. This manifests that Sb-O bonds are weaker than B-O bonds. In order to form a strong covalent bond, the participating orbitals of both the bond forming atoms should be comparable in size and energy and must have same symmetry with respect to the bond axis for the electron clouds to undergo a considerable overlap. Generally network bond strengths and glass forming-regions of heavy metal oxide glasses are small compared to conventional network formers. This is justified by the fact that heavy metal cation-oxygen bond strengths are relatively weaker, give rise to low fundamental vibration frequencies and thereby large IR transmission spectra. Another evidence is that in vitreous state B_2O_3 has interionic distance of 1.47 Å while in Sb_2O_3 it is about 2.0 Å [4,36]. Also in Sb_2O_3 glasses, the SbO_3 polyhedral chains are interlinked by weak secondary Sb-O bonds having lengths greater than 2.6Å [36]. In fact, the bond strengths of Sb-O and B-O are 89 ± 20 and 192.7 ± 1.2 kcal. mol^{-1} [36].

The dielectric constant values are also found to increase with increase of Sb_2O_3 content. The dielectric properties of materials are the inherent effect associated to the mechanism of polarization of the permanent and induced electrically charges by an external applied electric field. Here the KBS antimony glasses exhibits a relatively higher value of dielectric constant (ε) than the vitreous silica (ε = 3.8), soda-lime silicate (ε = 7.2) and borosilicate glasses (ε = 4.1–4.9) [37]. This is essentially due to the spontaneous high ionic polarization of Sb^{3+} ions along with its lone pair of $5s^2$ electrons (α_{Sb3+} = 1.111 $Å^3$) [35] under an applied electric field.

Due to non-centrosymmetric structure and high polarizability, antimony glasses are expected to possess large optical non-linearity [38]. The theoretical calculation of the metallization criterion (M) value (table 3) gives an indication of large NLO property of antimony glasses. It is well established that the third-order non-linear susceptibility (χ^3) value increases and M-value decreases [39]. The small metallization criterion means that the width of both valence and conduction bands become large, resulting in narrow band gap and increased tendency for metallization of the glass.

3.2 Photoluminescent properties of RE-doped antimony oxide glasses

Low phonon glasses doped with rare-earth (RE) ions have emerged as a significant category of solid-state luminescent materials with promising and ever-increasing applications as compact visible and NIR lasers, broad band amplifiers, light emitting devices, color display panels, optical data storage, sensors, optical communications etc [31,41,42]. Typically, the multiphonon relaxation rate is three orders of magnitude lower in low phonon fluoride glasses than in silicates. High phonon glasses can provide nonradiative decay pathways to suppress luminescence. On the contrary, low phonon glasses lower the non-radiative de-excitation processes that compete for upper state laser population. As an effect, many transitions which are non-observable in silicate glasses become active in fluoride glasses. This eventually led to obtain upconversion in low phonon glasses and to acquire short wavelength visible lasers upon pumping with NIR laser by involving two photons simultaneously [31].

Among the RE^{3+} ions capable of exhibiting photoluminescence upconversion, Sm^{3+} and Er^{3+} are the most suitable ones due to their favorable energy level structures [40,41] while Eu^{3+} is an important activator for down-shifted red light [42].

The antimony glass having composition (mol%) $15K_2O$-$15B_2O_3$-$70Sb_2O_3$ were doped with 0.3, 0.7 and 1.0 wt % Sm_2O_3 and Er_2O_3 (in excess) and studied for photonic applications. The ultraviolet-visible-near infrared (UV-Vis-NIR) absorption spectra of Sm^{3+}-doped glasses show six absorption bands from the ground state $^6H_{5/2}$ of Sm^{3+} ion (Fig. 7). The absorption bands give an approximation of the various energy levels of Sm^{3+} ion in antimony glass.

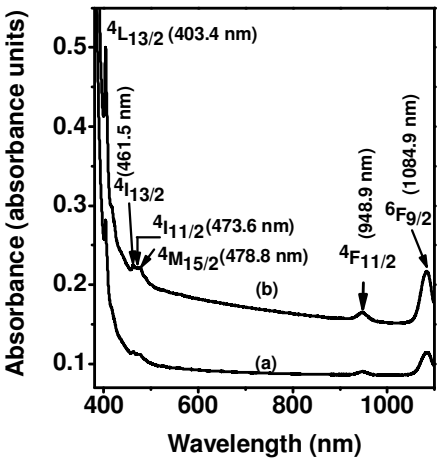

Fig. 7. Absorption spectra of (a) 0.3 and (b) 0.7 wt % Sm_2O_3 doped $15K_2O$-$15B_2O_3$-$70Sb_2O_3$ (mol %) glass in the range 380-1100 nm showing the various transitions arising from the ground state term $^6H_{5/2}$ (sample thickness: 2 mm).

The upconversion emission spectra of Sm_2O_3 doped KBS antimony glasses (Fig. 8) show three strong upconverted bands are observed to be centered at 566 (green, weak), 602 (orange, weak) and 636 (red, very strong) nm originated from the $^4G_{5/2} \rightarrow {}^6H_{5/2}$ ($\Delta J = 0$, zero-zero band, forbidden transition), $^4G_{5/2} \rightarrow {}^6H_{7/2}$ ($\Delta J = 1$, magnetic dipole transition) and $^4G_{5/2} \rightarrow {}^6H_{9/2}$ $\Delta J = 2$, electric dipole transition) anti-Stokes transitions respectively and a very weak red emission band at 649 nm due to $^4G_{5/2} \rightarrow {}^6H_{11/2}$ ($\Delta J = 3$, forbidden transition) upon excitation at 949 nm [17]. The ratio of intensities between the $^4G_{5/2} \rightarrow {}^6H_{9/2}$ and $^4G_{5/2} \rightarrow {}^6H_{7/2}$ transitions is used to determine the intensity parameter, η_{Sm} [17].

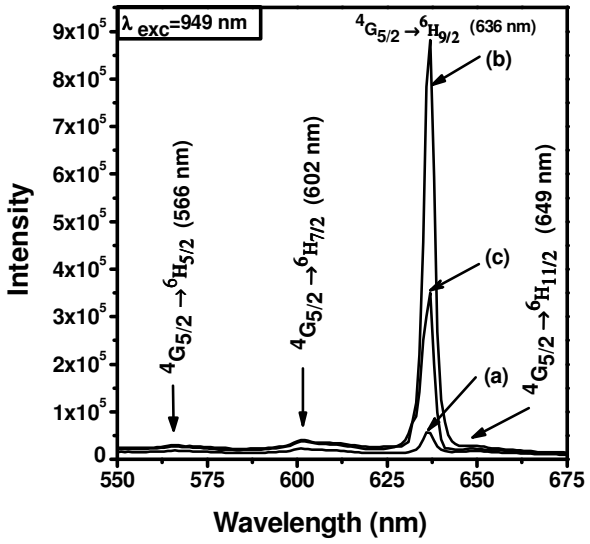

Fig. 8. Upconversion fluorescence spectrum of: (a) 0.3, (b) 0.7 and (c) 1.0 wt % Sm_2O_3-doped $15K_2O$-$15B_2O_3$-$70Sb_2O_3$ (mol %) glasses upon excitation at $\lambda_{ex} = 949$ nm radiation.

Similar emission bands at 566, 602 and 652 nm due to stokes transitions are also observed for normal (down conversion) fluorescence process upon excitation at 403 nm. For both cases, η_{Sm} reaches to a maximum at 0.7 wt% Sm_2O_3 concentration (12.02×10^{19} Sm^{3+} ions/cm^3). The upconversion can be explained considering the flowing processes operating between different energy levels thereby populating the metastable radiative storage level, $^4G_{5/2}$ [17]:

$$^6H_{5/2} \rightarrow {}^6F_{11/2} \text{ [Ground state absorption, GSA]}$$

$^6F_{11/2} \rightarrow {}^4I_{11/2}$ [Excited state absorption, ESA]

$(^6F_{11/2}, {}^6F_{11/2}) \rightarrow (^4I_{11/2}, {}^6H_{5/2})$ [Energy transfer, ET]

$(^6F_{9/2}, {}^6F_{9/2}) \rightarrow (^4G_{5/2}, {}^6H_{5/2})$ [Energy transfer, ET]

$(^4I_{9/2} \rightarrow {}^4G_{5/2})$ and $(^6F_{7/2} \rightarrow {}^6F_{11/2})$ [Resonant cross-relaxation, RCR]

In the case of upconversion, the intensity of $^4G_{5/2} \rightarrow {}^6H_{9/2}$ electric dipole transition is found to be about 23 times larger than that of $^4G_{5/2} \rightarrow {}^6H_{7/2}$ magnetic dipole transition. The full width at half maximum (FWHM) of the $^4G_{5/2} \rightarrow {}^6H_{9/2}$ transition at 0.7 wt % Sm_2O_3 is 4.2 nm. These results are quite contrary to the spectra obtained for conventional glasses where the $^4G_{5/2} \rightarrow {}^6H_{7/2}$ (orange) is usually the most intense one. These two facts illustrate the hypersensitive behavior of the $^4G_{5/2} \rightarrow {}^6H_{9/2}$ (red) transition and indicate that Sm^{3+} ions are in a highly polarizable chemical environment possessing a low symmetry geometric configuration. The calculated molar polarizability and refractive index of KBS antimony glass are found to be 9.598 $Å^3$ and 1.947 respectively. These values are much higher than that of silica glass (2.965 $Å^3$ and 1.46 respectively) [27]. So the strong upconverted red emission at 636 nm is ascribed to the forced electric dipole transition ($^4G_{5/2} \rightarrow {}^6H_{9/2}$) indicating the asymmetric geometrical environment of Sm^{3+} ion. The narrow FWHM means that Sm^{3+} environment distribution is small. Another reason for very strong red fluorescence may be attributed to the large non-linear optical (NLO) properties of antimony glasses [9]. Because additional electric field induced by NLO glass host may also make its contribution to the allowed electric dipole $^4G_{5/2} \rightarrow {}^6H_{9/2}$ transition which results in red fluorescence enhancement [17].

The other feature of the upconverted spectra is that the $^4G_{5/2} \rightarrow {}^6H_{9/2}$ transition bands at 636 nm have encountered a blue shift of 18 nm compared to the down conversion band at 652 nm for the same transition. This suggests that the upconverted Sm^{3+} ions are located in different unusual or distorted environments in KBS antimony glasses, i.e., they have different symmetry sites and orientation compared to those of Sm^{3+} ions participated in downconversion process [17]. The difference in the intensity of the yellow-green, orange and red fluorescence bands has happened due to the difference in the radiative transition rates from $^4G_{5/2}$ to the $^6H_{5/2}$, $^6H_{7/2}$ and $^6H_{9/2}$ energy levels respectively.

The Er_2O_3 doped antimony glasses show a total of eleven absorption bands from the ground state $^4I_{15/2}$ term. Upon excitation with 798 nm, The Er_2O_3 glass also exhibit two upconverted bands at 536 (green, medium), 645 (red, strong) nm due to $^4S_{3/2} \rightarrow {}^4I_{15/2}$ and $^4F_{9/2} \rightarrow {}^4I_{15/2}$ anti-Stokes transitions respectively and a weak band at 522 nm (green) due to $^2H_{11/2}$

$\rightarrow {}^4I_{15/2}$ transition (Fig 9). Similar emission bands are also observed in normal (down conversion) fluorescence spectra on excitation at 407 and 377 nm.

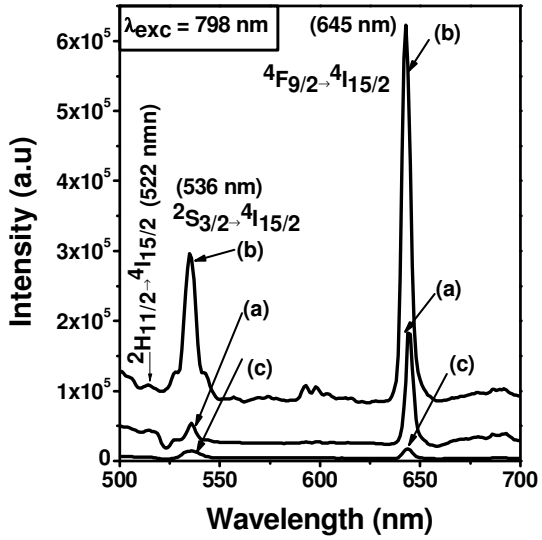

Fig. 9. Upconversion fluorescence spectra of: (a) 0.3, (b) 0.7, and (c) 1.0 wt % Er_2O_3-doped antimony glasses upon excitation at λex = 798 nm radiation.

The Er^{3+} ion in antimony glass show intense red upconversion on contrary to strong green upconversion usually observed in conventional glasses. This can be explained by considering the mechanism of upconversion. The strikingly greater red emission is possibly due to predominant cooperative energy transfer (CET) process operating between two neighbouring Er^{3+} ions from the very beginning even at low Er^{3+} ion concentration as [18]:

$$({}^4F_{7/2}, {}^4I_{11/2}) \rightarrow (2\ {}^4F_{9/2})$$

Secondly, Two excited Er^{3+} ions at $^4F_{7/2}$ and $^4I_{11/2}$ levels may also interact by resonant cross relaxation (RCR) process: ($^4F_{7/2} \rightarrow {}^4F_{9/2}$) and ($^4F_{9/2} \leftarrow {}^4I_{11/2}$) and thereby enhance the population of the $^4F_{9/2}$ state.

Thirdly, co-operative energy transfer (CET) phenomenon is accountable for the enhanced red emission as one Er^{3+} ion decays from the $^4S_{3/2}$ state to the $^4F_{9/2}$ state and a second ion is excited to $^4F_{9/2}$ state from $^4I_{9/2}$ state [18]:

$$({}^4S_{3/2}, {}^4I_{9/2}) \rightarrow (2\ {}^4F_{9/2})$$

The energy gaps of E_A ($^4S_{3/2} \rightarrow {}^4F_{9/2}$) and E_B ($^4F_{9/2} \leftarrow {}^4I_{9/2}$) are matched with a small red shift of 242 cm^{-1}. Based on the Frank-Condon principle and lattice relaxation theory, a small red shift between E_A and E_B is favorable for such type of energy transfer. The CET

process leads to improved population of the $^4F_{9/2}$ level and consequently superior red radiative emission. This fact indicates non-random distributed of E^{r3+} within the glass network even at a low concentration. The structure of the KBS antimony glass obviously plays a major role in suitable close distribution of the Er^{3+} ions within the interstitial spaces of the glass framework which facilitates the CET process irrespective of concentration. Another possible cross-relaxation energy transfer scheme includes [18]:

$$(^2H_{11/2}, {}^4I_{11/2}) \rightarrow (2{}^4F_{9/2})$$

The above CET mechanism leads to partial quenching of the green and improvement of the red emission. Thus the red emission is enhanced at the cost of the green emissions and hence the green emissions never exceed the red emission in antimony glasses. These processes are depicted in the energy level diagram of Er^{3+} (Fig. 10).

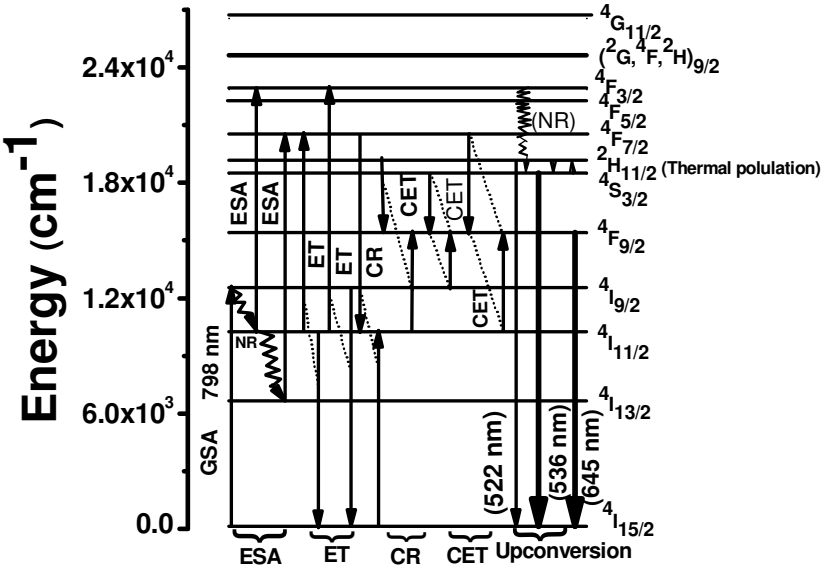

Fig. 10. Partial energy level diagram of Er^{3+} ion in $15K_2O$-$15B_2O_3$-$70Sb_2O_3$ (mol %) glass showing transitions in ground state absorption (GSA), excited state absorption (ESA), energy transfer (ET), cross relaxation (CR) and co-cperative energy transfer (CET) processes and upconversion fluorescence emissions at 522, 536 and 645 nm under excitation λ_{ex} = 798 nm radiation (R and NR represent the radiative and nonradiative transitions respectively).

The presence of OH groups may also assist in intensified red emission and dminished green emission. A similar observation has been recorded by De et al. [43]. The OH groups generate high energy vibrational modes (3259 cm^{-1}). The $^4I_{11/2}$ and $^4I_{13/2}$ are intermediate energy levels responsible for the green and red emissions respectively (see Fig. 10). The

energy gap between these two energy levels is ~ 3655 cm^{-1}. The high energy OH stretching vibration facilitates the $^4I_{11/2} \rightarrow {}^4I_{13/2}$ multiphonon relaxation process more efficiently compared to the intrinsic phonons (600 cm^{-1}) in bulk KBS antimony glass. Since the upconversion intensity depends on the population of the intermediate states, the presences of OH groups in the KBS antimony glass, therefore, results in an enhanced red emission and diminished green emission.

To study the downconversion (fluorescence) property of Eu^{3+} in antimony glass (Fig. 11), each of the KBS base glasses having composition (mol %) xK_2O-xB_2O_3-(100-2x) Sb_2O_3 glasses, where x = 15, 20 and 25 were doped with 0.7 wt% (in excess) with Eu_2O_3 (numbered as E-1, E-2 and E-3 respectively) and excited with 393 nm wavelength.

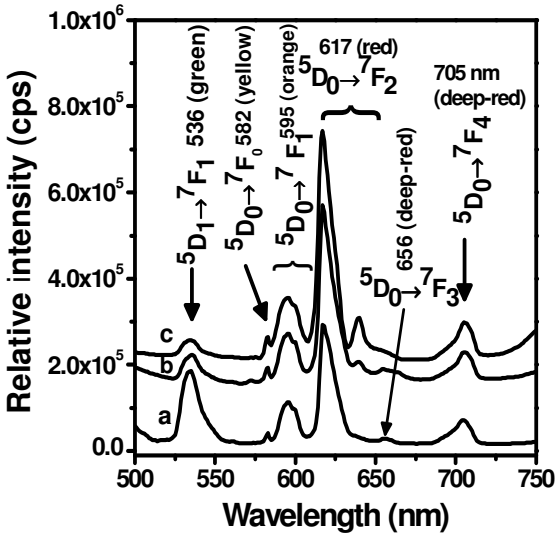

Fig. 11. Emission spectra of Eu_2O_3-doped KBS antimony glasses upon excitation at λex = 393 nm radiation: (a) E-1, (b) E-2, and (c) E-3.

In glassy materials, due the absence of a center of symmetry and long-range periodic arrangement of atoms, amalgamation of the 4f orbitals with an opposite parity orbitals take place. This rise to the ED transitions. The $^5D_0 \rightarrow {}^7F_2$ transition (electric dipole allowed) are forced by the crystal field environment in the vicinity of the Eu^{3+} ions. It is hypersensitive (ΔJ=2) transition and its intensity is very sensitive to the local environment. It shows two distinct main peaks (617 and 639 nm) due to the Stark splitting of the $^7F_2$ state, meaning that the Eu^{3+} ions are located in drastically disordered lower symmetry sites. The $^5D_0 \rightarrow {}^7F_1$

emission transition (magnetic dipole, (ΔJ=1)) of Eu^{3+} ions is forbidden under selection rules, has intensity independent of the host environment and can be used as a reference. It also exhibit small Stark splittings (595 and 600 nm) depending upon the ligand fields being experienced by them. The ratio IR = $I(^5D_0 \rightarrow {}^7F_2)/I(^5D_0 \rightarrow {}^7F_1)$ of the two integrated fluorescence intensities is commonly used as a measure of the asymmetry around the rare earth sites. Higher is its value, more would be the distortion from the inversion symmetry [16,44]. The value of IR is found to be 2.9, 4.0 and 4.3 for E-1, E-2 and E-3 respectively. This happens due to devitrification of the glasses (Fig. 1) with decreasing Sb_2O_3 content despite the increase in covalency and optical basicity. The ratio provides valuable information about the red color enrichment compared to the orange emission in developing strongly red luminescent optical systems.

The fluorescence spectra (Fig. 11) explicitly show the effect of lowering of phonon energy on the luminescence of Eu^{3+}. The $^5D_1 \rightarrow {}^7F_1$ green transition is observed only in low phonon glasses [42] and its intensity decreases with decreasing Sb_2O_3 content. Under 393 nm excitation, the Eu^{3+} ions are excited to $^5L_6$ level by ground state absorption (GSA) from which multiphonon relaxation takes place mainly resulting in the population of the $^5D_0$ and $^5D_1$ levels due to the low phonon energy of the glass. Multi-phonon relaxation from the $^5D_0$ level to the next lower level $^7F_6$ does not take place because of large energy difference (ΔE ~12290 cm^{-1}) between the two levels. Due to the low phonon energy of antimony glasses, minimum of three and twenty photons are required for bridging the $^5D_1 \rightarrow {}^5D_0$ and $^5D_0 \rightarrow {}^7F_6$ multiphonon relaxation process. Due to the high phonon orders (phonons $\geq$ 3) required, possibility of non-radiative multiphonon bridging decreases and results in $^5D_1 \rightarrow {}^7F_1$ (green) emission.

3.3 Plasmonic properties of nano metal (Au)-doped antimony oxide glasses

Metal-glass nanocomposites witness a historic background. The 4th Century A. D. Roman glass makers are originally credited to exploit the optical properties of metal nanoparticles for designing colourful medieval cathedral windows. In 1689, the German alchemist Johannes Kunckel first documented the history of the gold-ruby glass [45]. But modern works on preparation of metal-glass nanocomposites and scientific evaluation of their optical (plasmonic) properties were pioneered by Doremus around 1964 [46]. Thereafter the metal-glass nanocomposites kept receiving significant exposures and are currently occupy a significant area of material science and nanotechnology [47-53].

Preparation of nano metal doped conventional glass systems are not simple and demand multi-step techniques like sol-gel process, metal-dielectric co-sputtering deposition, direct metal-ion implantation, radiofrequency magneton sputtering, pulsed laser deposition, ion-exchange of thin plates followed by long time heat treatment at high temperatures in reducing (hydrogen) atmosphere or UV-light/X-ray/^{60}Co γ-radiation or high energy laser/synchrotron irradiation [45-53]. These methodologies face several limitations like tendency of sample damage due to exposure to high intensity radiation, formation of this layers of near-spherical nanoparticles restricted near the surface, applicable mainly to high melting and high softening glasses.

Dichroic glasses (reflect and transmit different light wavelengths) are generally produced by deformation of embedded spherical NPs into ellipsoidal NPs by intense irradiation with ultrashort laser pulses [54,55] or stretching metal-doped glasses in their softening range [56]. Formation of elliptical nanoparticles is an essential requirement to develop dichroic glasses [54,55] and but now it is a well acknowledged fact that prolate ellipsoid Ag NPs having an aspect ratio around 1.2 exhibits the phenomenon of dichroism [57].

Glasses containing nanosized metal NPs are increasingly being appreciated for their potential optoelectronic and photonic applications as optical data recording disks and memory devices, optical waveguides, optical switches based on their nonlinear optical properties, photochromatic and ophthalmic lenses, color glass recycling industry, three-dimensional multicolored industrial art objects, display devices, dichroic polarizers, etc [45-56]. In all these applications the size, shape, number density, and distribution of the nanoparticles critically determine performance and properties of the nanocomposites.

Glass is also often acknowledged as the ideal optically transparent matrix for encapsulating mono-disperse metal nanoparticles for practical applications. Metal-glass nanocomposites possess some inherent advantages like low cost of fabrication, the ease of processing in desirable shapes and sizes, high stability, thermal resistance, mechanical strength, ability to withstand high intensity radiation, preventing air oxidation of metal nanoparticles, etc. The possibility of of tailoring the behaviour of the encapsulating mother glass may creates possibility of unprecedented applications in nanotechnology. So a significant part of the applied research on glass is therefore currently focused on development of new cost-effective methodologies for large-scale production and controlling the behaviour of these glass-based nanomaterials.

Sb_2O_3 is a well known mild (selective) reducing agent (Sb^{5+}/Sb^{3+}, E^0 = 0.649 V). Here we exemplify, for the first time, how this property can be judiciously used for single-step synthesis of nano metal-glass nanocomposites (Au nanoparticles embedded glass) and RE-nano metal-glass hybrid nanocomposites (such as Eu^{3+} ions and Au nanoparticles co-embedded in antimony oxide glass in sub-section 3.4). Trivalent Au (introduced in the batch as $HAuCl_4.xH_2O$) is easily reduced to Au^0 (Au^{3+}/Au^0, E° = 1.498V) during the melting by trivalent Sb which itself is oxidized to pentavalent Sb. Thus a straightforward, low-cost strategy for the fabrication of bulk metal-glass nanocomposites in a single-step is exemplified without incorporation of any other external reducing agent. The overall reaction $3Sb^{3+} + 2Au^{3+} \rightarrow 3Sb^{5+} + 2Au^0$ is spontaneous reduction having E° = 1.05 V and a free energy (ΔG value) around -608 KJ. In principle, the E° of polyvalent elements in glass melts may be different from those in aqueous solutions and are temperature-dependent. But the E° values for antimony glasses and other required species at high temperature are not available in the literature, therefore for simplicity of understanding and considering the relative difference of E^0 values may be unaltered and that the trend or movement of alteration of the E^0 values of different redox pairs at high temperature of the glass melt would not be much different than in aqueous solution at room temperature, here we have used the room temperature E° for simple systems at equilibrium with air.

Noble metal nanoparticles of sizes below the electron mean free path incorporated in dielectrics exhibit the phenomenon of "**surface plasmon resonance**" (SPR) [3]. In presence of incident light, the free electrons in the conduction bands collectively oscillates to and fro with respect to the positive core and when the incident electromagnetic frequency is resonant with the frequency of oscillation, intense absorption bands in the visible-near-UV region results. In case of the small spherical particles this collective oscillation of the electrons is called the dipole plasmon resonance to distinguish from plasmon excitation that can occur in bulk metal or metal surfaces. The oscillation frequency is determined by four factors: the density of electrons, the effective electron mass, and the shape and size of the charge distribution. In addition, the surrounding dielectric medium also exerts considerable influence [3,58]. So the position of the SPR band in these nanocomposites may be tuned by monitoring the refractive indices of the glass matrices, size, concentration and interparticle distance of the nanoparticles [3,58].

To study the effect of Au concentration on SPR band in monolithic K_2O-B_2O_3-Sb_2O_3 (KBS) glasses, the following compositions were selected. Some of their properties are also listed in Table 4.

Table 4. Composition and some properties of Au^0-antimony glass dichroic nanocomposites

Sample identity no.	Concen-tration of Au (wt %)[a]	Color of transmitted light	Color of reflected light	SPR band position, λ_{max} (±1, nm)
B	-	Yellow	Yellow	-
G1	0.001	Blue	Brown	610
G2	0.003	Blue	Brown	610
G3	0.1	Blue	Brown	680
G4	0.3	Blue	Reddish-brown	681

[a] Base glass (B) composition (mol %): $15K_2O$-$15B_2O_3$-$70Sb_2O_3$

All the Au-doped antimony glass nanocomposites are dichroic, that is, they transmit blue light and reflect the brown light (Fig. 12). The intensity of dichroism increases with increase in Au concentration.

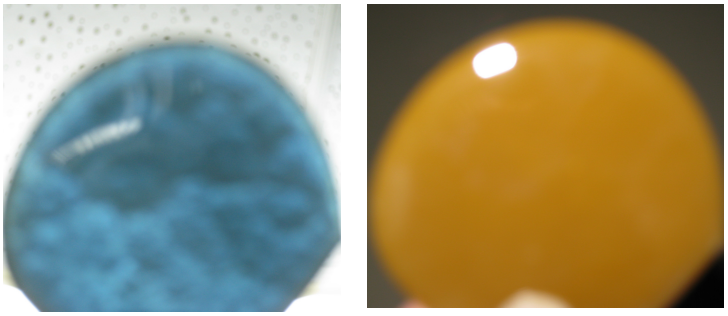

(a) (b)

Fig. 12. Photograph showing dichroic behavior of Au-antimony glass nanocomposites: (a) blue in transmitted light and (b) brown in reflected light.

The dichroism possibly originates due to elliptical Au nanoparticles in these nanocomposites, as seen from the TEM image (Fig. 13a). The representative TEM image (Fig. 13a) (of nanocomposites G-2) shows of the Au^0 NPs nanoparticles majority of which have elliptical. The major axis (diameter) of the NPs ranges from 3 to 13 nm (± 3 %) while the average aspect ratio of the elliptical Au^0 NPs is found to be about 1.2. Here the mechanism of deformation or the formation of elliptical nanoparticles by the simple single-step melt-quench process is probably due to the influence of the high viscosity of the molten Sb_2O_3 based matrix on the Au^0 colloids. The SAED image shows the presence of (111) and (200) crystallographic planes of Au^0 and consents well with XRD patterns.

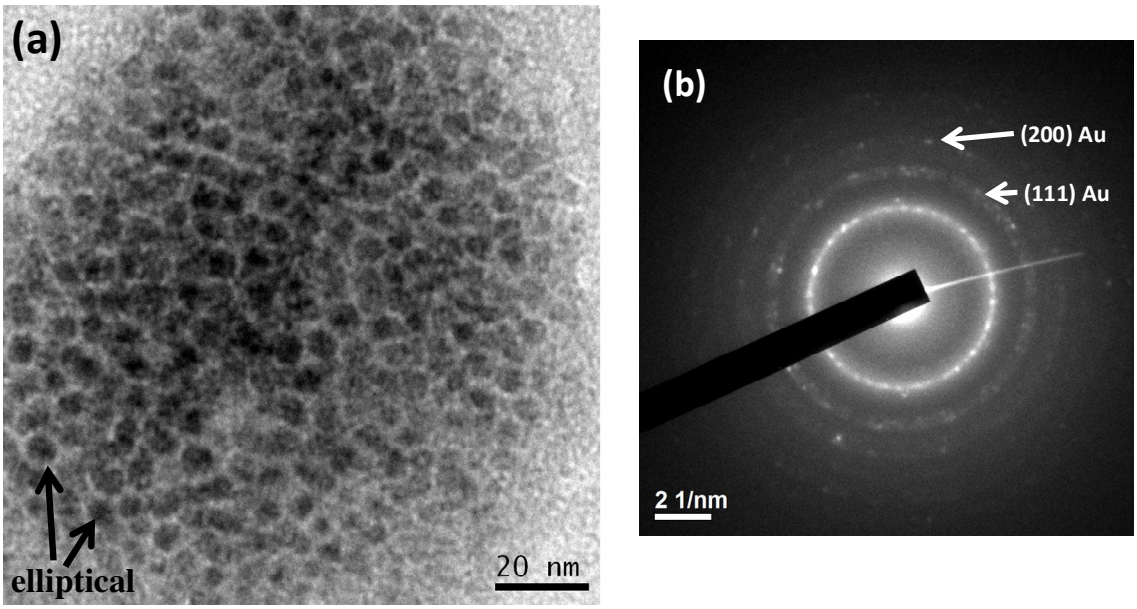

Figure 13 (a) TEM image of nanocomposite G-2 and (b) the SAED pattern of a Au nanoparticles (for composition see Table 4).

Prolate ellipsoid metal NPs are known to exhibit the phenomenon of dichroism due to the difference in polarizations along the major (longitudinal) and minor (transverse) axes of a polarizable ellipsoidal nanoparticle in presence of electromagnetic wave [54-57]. It has also been observed that for such elliptical (elongated) Ag NPs the SPR peak obtained from the interaction of transversely polarized light is different from the SPR peak position acquired in presence of longitudinally polarized light corresponding to transverse and longitudinal electron oscillations (with respect to the particle principal axis) respectively [54-57]. So it is possible to selectively excite each of them by using light with oscillating electric field parallel and perpendicular to the major axis of the ellipsoids (polarization dependent optical response), consequently such dichroic nanocomposites are therefore possible candidates for displays or encoding security systems and for making dichroic glass polarizers [3,54,54].

The XRD spectra provide another evidence of the presence of Au nanocrystals in the nanocomposites (Fig. 15). In the XRD band (curve-a), particularly the hump between 25° to 35° indicates its amorphocity due to presence of uncrystallized Sb_2O_3 or other constituents in the base glass (B). The sharp peak at 2θ = 38.4021° (d = 2.34216 Å) and 44.1634° (d = 2.04906 Å) (curves b-e) is assigned as (111) and (200) diffractions of fcc Au^0 nanoparticles (JCPDS, card file no. 4-0784) embedded within the antimony borate glass matrix.

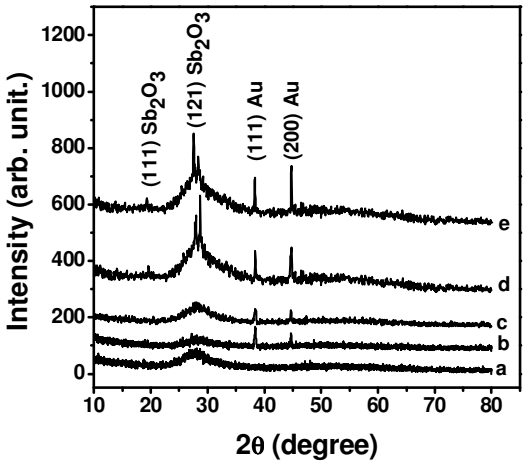

Fig. 15. XRD pattern of (a) base glass B having composition (mol %): $15K_2O$-$15B_2O3$-$70Sb_2O_3$, (b) G1, (c) G2, (d) G3, and (e) G4 showing nano Au^0 and crystallized valentinite type phases of Sb_2O_3 (for composition see Table 1).

In the XRD spectra (Fig. 15), the sharp peaks at 2θ = 19.5366º (d = 4.54013 Å), 25.5436° (d = 3.48443 Å) and 28.5159º (d = 3.12764 Å) corresponds to (110), (111) and (121) diffractions of valentinite form of Sb_2O_3 crystals (JCPDS, card file no. 11-689) created within the antimony borate glass matrix due to crystallization of some Sb_2O_3 of the matrix by very high concentrations of metallic Au precipitated throughout the body of the glass and acting as heterogeneous nuclei and catalyzing the crystallization of Sb_2O_3 in K_2O-B_2O_3-Sb_2O_3 system [60]. The representative FESEM images (Fig. 16 a and b) of nanocomposites G1 and G3 shows distinct microstructure tuning with increasing Au concentration. Such crystallization results because the (111) plane of Au crystal resembles the (012) and (200) planes of valentinite with a disregistry of approximately 14% and 4% respectively. This falls well within the maximum disregistry of 10 to 15 % suggested for good nucleation catalysis [61].

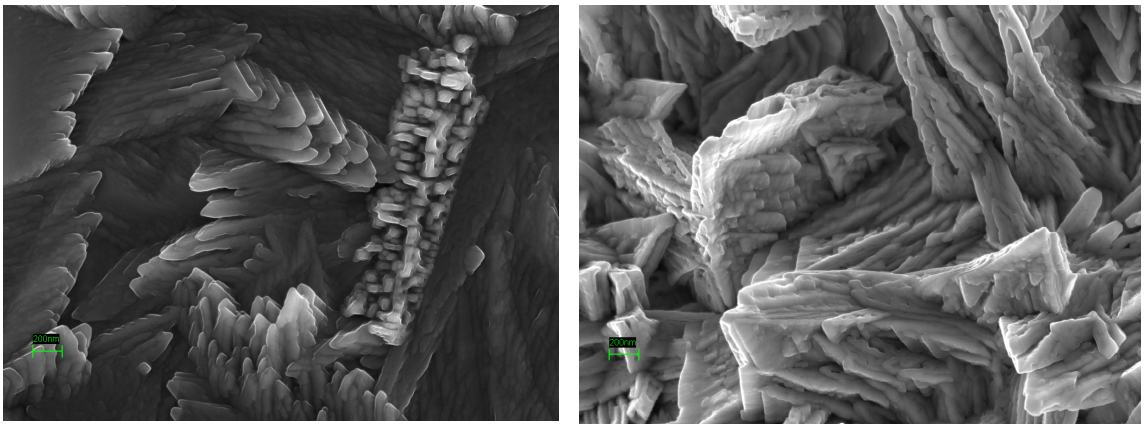

Fig. 16. Representative FESEM images of (a) nanocomposite G1 showing hand-ike microstructure and (b) nanocomposite G3 showing rugged-cliff like microstructure. (Both scales 200 nm; for composition see Table 4).

The UV-Visible absorption spectrum (Fig. 17) is one of the most sensitive tools to detect the formation of plasmonic metal NPs. The UV-Vis-NIR absorption spectrum of the undoped glass (curve-a) shows absence of any features but the absorption spectra of the Au doped NCGs (curves b-e) display well-defined broad plasmon (SPR) absorption bands (610-681 nm) characteristic of nano sized Au^0.

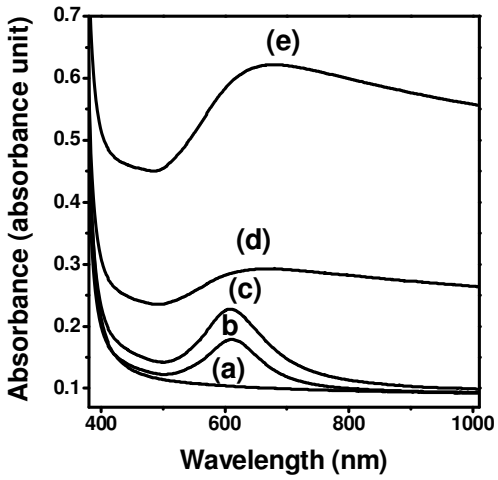

Fig. 17. UV-Vis absorption spectra of (a) based glass B and nanocomposites (b) G1, (c) G2, (d) G3 and (e) G4 (for composition see Table 4).

Typically the SPR for nano Au in sodaline silicate glass (refractive index ~ 1.5) appear around 520 nm for near-spherical nanoparticles. But here in KBS antimony glass the maxima of the plasmon peaks (λ_{max}), listed in Table 4, experience a distinctive red-shift towards higher wavelength (from 610 nm to 681 nm) with increase in Au^0 concentration (from 0.001 to 0.3 wt %). At higher concentration the SPR band gradually broadened and their tails have extended up to 1100 nm. The curves are very similar to that obtained by Pardiñas-Blanco (Fig. 3.11) [62]. This type of complex system where a high refractive index dielectric matrix encompasses closely spaced elliptical nanoparticles having electromagnetic coupling, the need arises for theory that can describe the electrodynamics of such nanoparticles [63].

According to the Mie theory, for a collection of small spherical non-interacting metallic spheres (low particle density) in the quasi-static regime of radius (R) having a dielectric function (complex) that depend on the angular frequency of light ω, $\varepsilon_{Au}(\omega) = \varepsilon_1(\omega) + i\varepsilon_2(\omega)$, embedded in a medium of dielectric constant ε_m (real), and sizes much smaller than the wavelength of light ($D = 2R << \lambda$) (about 25 nm for gold particles), only the dipole oscillations contribute significantly and the extinction (= absorption + scattering) coefficient C_{ext} is given by [63]:

$$C_{ext} = [24\pi^2 R^3 \varepsilon_m^{3/2} / \lambda] \times [\varepsilon_2 / \{(\varepsilon_1 + 2\varepsilon_m)^2 + \varepsilon_2^2\}] \qquad (5)$$

where *N* is the number of particles, V_{np} the volume of each particle in the quasi-static regime ($V_{np} = 4\pi R^3/3$). The real (ε_1) and imaginary (ε_2) parts of the dielectric function $\varepsilon_{Au}(\omega)$ may be expressed according to the Drude model as [63,64]:

$$\varepsilon_1(\omega) = \varepsilon_\infty - \omega_p^2/(\omega_p^2 + \omega_d^2) = \varepsilon_\infty - \lambda^2/(\omega_p^2 + \omega_d^2) \qquad (6)$$

$$\varepsilon_2(\omega) = \omega_p^2\omega_d/\omega(\omega^2 + \omega_d^2) = \lambda(\lambda^2 + \lambda_d^2)/\lambda_p^2\lambda_d \qquad (7)$$

where ε_∞ is the high-frequency value of the dielectric function or optical dielectric function of the metal and $\omega_p = 2\pi c/\lambda_p = (n_{eff}\, e^2/m_{eff}\, \varepsilon_o)^{1/2}$ is the metal's bulk plasma frequency while λ_p is the metal's bulk plasma wavelength, $\omega_d = V_F/R_{bulk}$ is the damping or relaxation frequency, n_{eff} is the free electron concentration in the metal, m_e is effective mass of conduction electrons, V_F is the Fermi velocity of the metallic electrons, R_{bulk} is the mean free path of the oscillating conduction band electrons and ε_o is vacuum dielectric constant or free space permeability. Such particles will retaliate as dielectric media in an optical field. If ε_i is very small or weakly dependent on ω then, from Eq. (5), the absorption maximum corresponding to the resonance condition is produced when $\varepsilon_1 = -2\varepsilon_m$, leading to a disappearing

denominator. Hence, a SPR absorption is produced at optical frequency ω at which the resonance condition $\varepsilon_1 = -2\varepsilon_m$ is fulfilled [63,64].

When $\omega_p >> \gamma$ (damping), the SPR absorption maxima λ_{max}, is susceptible to the changes of refractive index, n_m of the surrounding medium as [63,64]:

$$\lambda_{max} = \lambda_p^2 (\varepsilon_\infty + 2\varepsilon_m) = 2\pi c\, m_{eff}\, \varepsilon_o\, [(\varepsilon_\infty + 2n_m^2)]^{1/2} / n_{eff}\, e^2 \qquad (8)$$

where $n_m = (\varepsilon_m)^{1/2}$ Thus, the SPR peak exhibits a red-shift with increase in medium refractive index [63,64].

To study the effect of medium refractive index on plasmon band of Au in monolithic K_2O-B_2O_3-Sb_2O_3 (KBS) glasses, the following compositions were selected (Table 5).

Table 5. Composition and some properties of Au^0-devitrified antimony glass dichroic nanocomposites

Nano-composite no.	Glass composition (mol %)			Concentration of Au (wt%)[a]	Refractive index	SPR maxima, λ_{max} (nm)	Transmitted color	Reflected color
	K_2O	B_2O_3	Sb_2O_3					
G5	10	10	80	0.003	2.0006	611	Green	Reddish-brown
G6	15	15	70	0.003	1.9477	610	Bluish green	Brown
G7	20	20	60	0.003	1.8925	599	Blue	Brown
G8	25	25	50	0.003	1.8349	587	Bluish-violet	Brown

Since the Au concentration remains constant, the tuning of the SPR wavelength is essentially accomplished by varying the content of high refractive index Sb_2O_3. With increase of refractive index of the matrix from 1.8349 to 2.0006, there is a red shift of 24 nm of SPR band of Au. This results in different colored nanocomposites (Fig. 18).

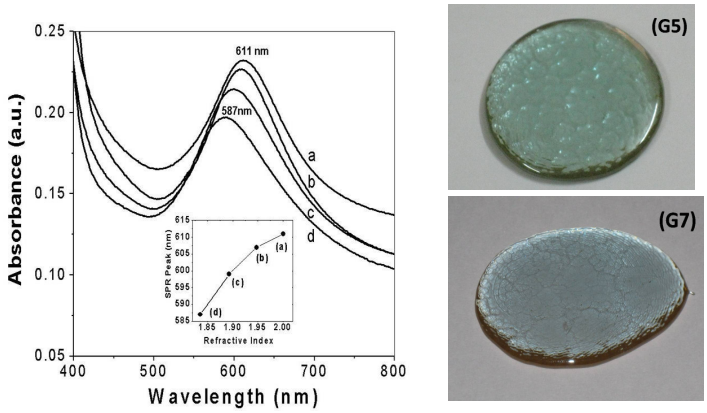

Fig. 18. UV-Vis absorption spectra of nanocomposites (a) G5, (b) G6, (c) G7, and (d) G8. Inset plot shows the red shift of Au^0-SPR band with increase in refractive index of the embedding matrix. Photographs show the transmitted color of as-prepared G5 (green) and G7 (blue) (for composition see Table 5).

The effects of the medium refractive index on the optical properties of noble metal nanostructures have predominantly captured rising fundamental and technological interest in recent times. Consequently, tuning of the SPR bands of Au and Ag nanoparticles have been experimentally in a variety of surroundings including solutions, polymers and sol-gel derived hybrid matrices [3,63, 65,66]. Most of metal-glass composites to date have been comprised of spherical NPs inserted within silicate or phosphate matrices where to make a wide variation of refractive index is very difficult. Consequently, refractive index controlled plasmon tuning has hardly been realized within glass matrices. But antimony glasses provide the unique opportunity of plasmon tuning by controlling the fraction of Sb_2O_3 (high refractive index material) in glasses.

Within the dipole approximation, the Gans theory, which is an extension of Mie theory, is applicable for small ellipsoidal (prolate and oblate) particles. Here the plasmon resonance may split into two distinct modes depending on the aspect ratio. Such splitting is the result of surface curvature which decides the restoring force or depolatization effect that acts on the resonating conduction band electrons. Consequently, the extinction cross-section, C_{ext}, of ellipsoidal particle is directly proportional to its imaginary part of polarizability, α_{ED} as [63,64]:

$$C_{ext} = 2\pi n_h I(\alpha_{ED})/\lambda \quad (9)$$

where

$$\alpha_{ED} = V\varepsilon_m \frac{\varepsilon_{Au} - \varepsilon_m}{\varepsilon_m + L_j(\varepsilon_{Au} - \varepsilon_m)} \quad (10)$$

j = x, y, z denotes the principal axes of the ellipsoid, the volume of the ellipsoidal nanoparticle, $V_{ED}=(4R_xR_yR_z)/3$ and Lj are depolarization factors given by [3,63,64]:

$$L_x = [(1-e^2)/e^2][-1 + (1/2e)\ln(1+e)/(1-e)] \quad (11)$$

$$L_{y,z} = (1-L_x)/2 \quad (12)$$

where $e = [1-(b/a)^2]^{1/2}$ is the eccentricity of the ellipsoid. For the degenerate case of a sphere e = 0, or radius $R_x = R_y = R_z$, $Lj = 1/3$. under these conditions, the birefringence disappears. Thus oriented ellipsoids exhibit strong polarization-dependent optical spectra. Simply,

nanocomposites exhibits dichroic behavior, that is, one color in the transmitted light and a different color in the reflected light [63]. Consequently, the new SPR position is:

$$\varepsilon_{Au} = (-1/Lj + 1)\ \varepsilon_m, \qquad (13)$$

It is thus established SPR is intimately controlled by the nanoparticle size, shape, refractive index of the dielectric host (here glass) and other proximal NPs.

3.4 Nano Metal: Rare Earth Ion- Antimony Glass Hybrid Nanocomposites for Enhanced Photoluminescence Applications

Nano metal: RE ion-glass hybrid nanocomposites have very recently received startling importance as potential candidates of nanophotonic applications. These intelligent solid state materials exhibiting enhanced photoluminescence are promising for applications in some current thrust areas of materials science like advanced displays, light emitting diodes, solar cells (energy harvest) and communications [3].

SPR by metallic nanoparticles not only result in strong absorption bands but also tremendous enhancement of the local electromagnetic field and intense light scattering [3]. The local electromagnetic field enhancement may be so strong that luminescent species in the vicinity of the plasmonic noble metal nanoparticle (~ 10 nm apart) may feel up to a 100 times more intense field as opposed to the direct excitation in a plasmon-free environment [67]. These enhanced near-fields around metallic nanostructures have already fostered a variety of intriguing applications such as non-linear optics, surface-enhanced Raman scattering (SERS), single-molecule detection (spectroscopy), nano-metal enhanced fluorescence (NMEF) and phosphorescence (NMEP), etc [68].

Originally inspired by the discovery of SERS in 1974, Malta et al. [69] first demonstrated the luminescence enhancement of the Eu^{3+} ions by silver-nanoparticles in fluoro-borate glasses prepared by conventional melting and annealing technique which incorporated a small quantity of reducing agent (1.5-3 wt% Sb_2O_3). The phenomenon was explained as silver plasmonic enhancement effect and long range electromagnetic interactions associated with SPR. Their results were further established by Hayakawa et al [70] who observed luminescence enhancement of Ag NPs–Eu^{3+} ions co-doped sol-gel derived silica glasses (synthesized by using partially hydrolyzed tetrakis(hydroxymethyl) phosphonium chloride as the reducing agent and annealing in hydrogen atmosphere) and found that irrespective of Ag concentration, the decay from the $^5D_0$ level of Eu^{3+} almost have the same life-time.

Thereafter, several researchers worldwide took up NMEL studies of Er^{3+}, Sm^{3+}, Tb^{3+}, Eu^{3+}, Dy^{3+}, etc ions by monometallic Au or Ag NPs in glasses and other dielectric offering the possibilities of plamon induced nanphotonics engineering [67,71-77]. However, the simultaneous studies also led to several controversies related to metal–RE interactions in a dielectric host and the mechanism of photoluminescence enhancement.

Strohhöfer and Polman [71] reported the photoluminescence enhancement of Er^{3+} ions implanted in boro-silicate glasses that had been subjected to $Na^{+} \leftrightarrow Ag^{+}$ ion exchange via absorption at a defect related to a pair of silver ions/atoms and energy transfer towards Er^{3+}. Matarelli et al. [72] described electric-dipole induced energy transfer process from ionic silver aggregates, particularly dimmers, accounting the enhancement of 1.52 μm emission of Er^{3+} in silver-doped silicate glasses fabricated by ion-exchange technique. These contrasting conclusions are probably because when metal ions are introduced in glasses by conventional ion-exchange or ion-implantation they are very mobile and with heat treatment have a strong tendency to aggregate. This results not only in formation of nanoparticles, but single ions, cluster of few atoms (dimers, trimers, etc.), and other luminescent optical centers, examples are Ag^{+}, $(Ag_2)^{+}$, $(Ag^{+})_2$, $(Ag_3)^{2+}$ for silver. Moreover low temperature small annealing schedules results in large fraction of the metal to form sub-nm aggregates that are two small to have a continuous density of states necessary for evolution of SPR typical of larges free-electron metal nanoparticles.

Recent studies of nanometal enhanced rare-earth luminescence in glasses have revealed plasmonic induced local field enhancement as the primary cause particularly when the pumping excitation or emission is resonant or lies near the SPR wavelength [73-77]. Energy transfer from metal nanoparticles has also been regarded as a contributing effect when excitation or emission is non-resonant with SPR provided the chosen metal concentration is below the threshold concentration beyond which quenching may occur [73-77].

Although, the luminescence of Eu^{3+} ion by gold and silver nanoparticles have been studied in bismuth and tellurite glasses [75,76], but there is no report of nanometal enhanced Eu^{3+} luminescence in antimony glasses. The selective reduction capability of Sb_2O_3 enables the synthesis of nano Au:Eu^{3+}-KBS glass nanocomposites in a single-step. Although Sb_2O_3 reduces Au(III) to Au^{0}, but its reducing potential is not strong enough to reduce Eu^{3+} to its lower valent states $E^{o}_{Eu3+/Eu0}$ = -1.991 V, $E^{o}_{Eu3+/Eu2+}$ = -0.36 V and $E^{o}_{Eu2+/Eu0}$ = -2.812 V] [78].

The effect of Au nanoparticles of various concentrations on the luminescence (downconversion) of Eu^{3+} ion in KBS antimony glass, having base glass composition (mol%) $15K_2O$-$15B_2O_3$-$70Sb_2O_3$ is shown in Fig. 19.

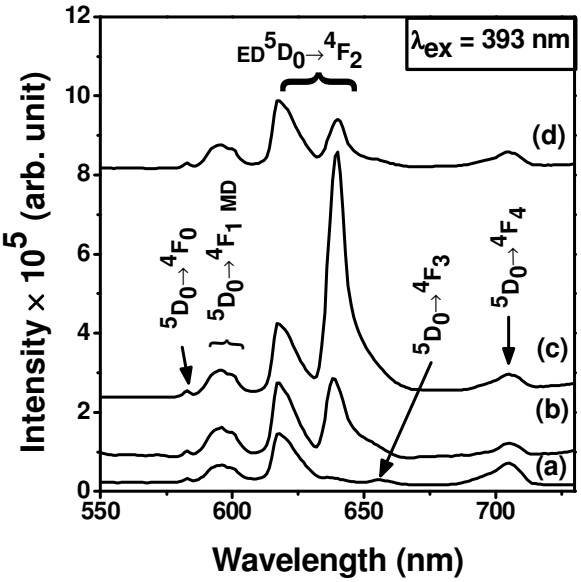

Fig. 19. Fluorescence spectra of (a) 0.3 wt% Eu^{3+}-doped, (b) 0.003 wt% Au and 0.3 wt% Eu^{3+}-codoped, (c) 0.03 wt% Au and 0.3 wt% Eu^{3+}-codoped and (d) 0.3 wt% Au and 0.3 wt% Eu^{3+}-codoped KBS glass, under excitation wavelength at λex = 393 nm. The bases of the emission curves b, c and d have been uplifted for clear visibility

The $^5D_0 \rightarrow {}^7F_1$ orange transitions are magnetic-dipole (MD) allowed and are not much sensitive to changes in the crystal field environment of the host matrix. But $^5D_0 \rightarrow {}^7F_2$ red emission transitions are allowed by electric-dipole (ED) and are influenced by the crystal field environment in the vicinity of the Eu^{3+} ions. Their amplitudes are susceptible to changes in the polarizability of the ligand and reduction of the local symmetry around the Eu^{3+} ions. The formation of Au nanocrystallites introduces local crystalline environment and perturbs the local site symmetry resulting in well resolved Stark's splitting of the hypersensitive ($\Delta J=2$) $^5D_0 \rightarrow {}^7F_2$ red emission transition (617 and 640 nm) due to crystal field effect. The principal result of the current study is that the 640 nm (deep-red) fluorescence of Eu^{3+} initially drastically enhances in presence of Au^0 NPs and then diminishes at very high Au concentration. The enhancement of ED transition is as high as 8 folds while the MD transition is much less affected. This indicate that Eu^{3+} ions are located at least into two different crystalline environments, namely, a clustered crystalline environment (due to

coalescence of some Au nanoparticles) and dispersed one. The emission spectra are indicative of the rare-earth sites. Earlier Kassab et al [75,76] have showed that the dominant hypersensitive $^5D_0 \rightarrow {}^7F_2$ electric dipole (red) transition is increased by 10 fold by Au nanoparticles while the less sensitive $^5D_0 \rightarrow {}^7F_1$ magnetic dipole (orange) transition is enhanced only by 5 folds.

We believe that the enhanced luminescence is primarily due to local field enhancement (LFE) around the Eu^{3+} ions induced by SPR of Au NPs. The SPR results in generation of electromagnetic waves at the interface of the dielectric medium and metal. Concentration of these waves results in enhanced local fields around the metal nanoparticles. The enhancement is dramatic at the interparticle region called "hot spots". Any luminescent species at the vicinity of metal nanoparticles or located at the "hot spots" experience enormous increase in their excitation rate compared to the incident field. Consequently, their emission also drastically increases. At very high Au concentration there is quenching due to reverse energy transfer from Eu^{3+} to Au and plasmonic re-absorption.

According to the classical electromagnetic theory, local field enhancement factors for ellipsoidal particles are given as [79]:

$$\eta_x(\omega) = \frac{\varepsilon_m L_{LR}}{\varepsilon_{Au} - \varepsilon_m + L_{LR}\left(\varepsilon_m + i\,\frac{4\pi^2 V}{\lambda^3}\,(\varepsilon_m - \varepsilon_{Au})\right)} \qquad (14)$$

$$\eta_{y,z}(\omega) = \frac{\varepsilon_m \frac{2L_{LR}}{L_{LR} - 1}}{\varepsilon_{Au} - \varepsilon_m + \frac{2L_{LR}}{L_{LR} - 1}\left(\varepsilon_m + i\,\frac{4\pi^2 V}{\lambda^3}\,(\varepsilon_m - \varepsilon_{Au})\right)} \qquad (15)$$

where η_x, $\eta_{z,y}$ are the enhancement factors for the electric field vectors directed along the axis of revolution of ellipsoid (x) and perpendicular to this axis, respectively. L_{LR} is lightning rod factor due to enhanced filed contribution from sharp edges (or rough surfaces) of anisotropic nanostructures. The field enhancement factor, η is defined as the ratio of the amplified local field and the incident field, $|\eta(\omega)| = |E_{loc}| / |E_i|$.

We may eliminate the possibility of energy transfer from Au nanoparticles to Eu^{3+} ions as the excitation wavelength does not overlay the SPR absporption. Moreover, our luminescence experiments indicated the absence of any other optical centers. Apart from the Eu^{3+} emission bands, any other emission band was not obtained under excitation at various wavelengths which could be attributed to any ionic species of Au. This is because we used

exceedingly large quantity of reducing agent (89.25 wt% Sb_2O_3) compared to $HAuCl_4.H_2O$ (0.003-0.3 wt% Au).

The Au:Sm^{3+}-KBS and Au:Er^{3+}-KBS glasses synthesized by similar single step technique also exhibit intensified upconversion emissions due to local field effect of Au nanoparticles [21,22].

4. Conclusions

A novel series of antimony trioxide based monolithic glasses and monolithic devitrified glasses in the systems K_2O-B_2O_3-Sb_2O_3 (KBS) having low melting, low softening point, high thermal expansion and high dielectric constant are developed. Their properties are explained with evaluation of fundamental properties like covalent character and optical basicity. The glasses are impending candidates for electrical packaging industry. It is also established that they possess low phonon energy (600 cm^{-1}) comparable to fluoride glasses. On doping with Sm_2O_3 they emit extraordinary red upconverted light, with Er_2O_3 both intense green and red upconversion emissions are observed with NIR excitations. On doping with Eu_2O_3, green, orange and red down-shifting emissions are exhibited upon UV excitation the intensity of which is dependent on the concentration of Sb_2O_3 in the glasses. RE-doped antimony glass are found to be promising candidates for visible lasers and display applications and possible substitutes for fluoride glass. The mild (selective) reducing property of Sb_2O_3 enables the single-step synthesis of nano metal-glass nanocomposites and RE-nano metal-glass hybrid nanocomposites for the first time. Dichroic Au-doped antimony glass nanocomposites exhibiting shape, size, inter-particle distance and refractive index dependent plasmon absorption bands may be used for various plasmonic applications. Namo metal- rare earth ion hybrid antimony glass nanocomposites exhibiting intense photoluminescence plasmon induced due to local field enhancement of metal nanoparticles, may be used for various nanophotonic applications promising new materials for various nanophotonic applications, like in solar cells, light emitting diodes (LEDs), advanced displays, etc. These pioneering findings so-far explored in rare-earth doped Sb_2O_3 glasses and Sb_2O_3 glass based nanometal-glass nanocomposites are expected to set a new prototype field of unusual glasses.

Acknowledgements

TS expresses her sincere gratitude to Council of Scientific and Industrial Research (CSIR-India) for award for NET-SRF research grant under sanction number 31/015(0060)/2007-EMR-1. The authors thank the technical supports provided by the infrastructural facility of CGCRI, Kolkata and TEM facility at IACS, Kolkata.

References

[1] Yamane, M. and Asahara, Y. (2000). *Glasses for Photonics*. Cambridge University Press.

[2] Gonella, F. and Mazzoldi, P. (2000). "Metal Nanocluster Composite Glasses." In: *Handbook of Nanostructured Materials and Nanotechnology.* Nalwa H. S., Ed., vol 4, San Diego, Academic Pres,.

[3] Prasad, P. N. (2004). *Nanophotonics.* New Jersey, Wiley, pp. 129-151.

[4] Vogel, W. (1992). *Glass Chemistry.* Berlin, Springer-verlag.

[5] Zachariasen, W. H. (1932). "The atomic arrangements in glass." *Journal of the American Chemical Society* 54, 3841-3851.

[6] Kordes, E. (1939). "Physikalische-chemische untersuchungen über feinbau von gläsern, III (Physicochemical researches on fine structure of glasses: III Binary and pseudobinary glasses without appreciable packing effect)." *Zeitschrift für Physikalische Chemie B* 43, 173-190.

[7] Hedden W. A. and King, B. W. (1956). "Antimony oxide glasses." *Journal of the American Ceramic Society* 39, 218-222.

[8] Bednarik J. F. and Neely, J. A. (1982). "Thermal properties of single component antimony oxide glass." *Physics and Chemistry of Glasses* 23, 204-205.

[9] Terashima, K., Hashimoto, T., Uchnio, T., Kim, S. and Yoko, T. (1996). "Structure and nonlinear optical properties of Sb_2O_3-B_2O_3 binary glasses." *Journal of the Ceramic Society of Japan* 104, 1008-1014.

[10] Nalin, N., Poulain, M. J., Poulain, M. A., Ribeiro, S. J. L. and Messaddeq, Y. (2001). "Antimony oxide based glasses." *Journal of Non-Crystalline Solids* 284, 110-116.

[11] Nalin, M., Messaddeq, Y., Ribeiro, S. J. L., Poulain, M., Briois, V., Brunlkaus, G., Rosenhahn, C., Mosel, B. D. and Eckert, H. (2004) "Structural organization and thermal properties of the Sb_2O_3–$SbPO_4$ glass system." *Journal of Materials Chemistry* 14, 3398-3405.

[12] Holland, D., Hannon, A. C., Smith, M. E., Johnson, C. E., Thomas, M. F. and Beesley, A. M. (2004) "The role of Sb^{5+} in the structure of Sb_2O_3-B_2O_3 binary glasses-an NMR and Mössbauer spectroscopy study." *Solid State Nuclear Magnetic Resonance* 26, 172-179.

[13] Chatlani S. and Shelby J. E. (2006). "Properties of arsenic and antimony borate glasses." *Physics and Chemistry of Glasses: European Journal of Glass Science and Technology B* 47, 288-293.

[14] Zhang, B., Chen, Q., Song, L., Li, H., Hou, F. and Zhang, J. (2008). "Fabrication and properties of novel low-melting glasses in the ternary system ZnO-Sb_2O_3-P_2O_5." *Journal of Non-Crystalline Solids* 354, 1948-1954.

[15] Som, T. and Karmakar, B. (2010). "Structure and properties of low-phonon antimony glasses and nano glass-ceramics in K_2O-B_2O_3-Sb_2O_3 system." *Journal of Non-Crystalline Solids* 356, 987-999.

[16] Som, T. and Karmakar, B. (2010). "Optical properties of Eu^{3+}-doped antimony-oxide-based low phonon disordered matrices." *Journal of Physics: Condensed Matter* 22, 035603 (11 pages).

[17] Som, T. and Karmakar, B. (2008). "Infrared-to-red upconversion luminescence in samarium-doped antimony glasses." *Journal of Luminescence* 128, 1989–1996.

[18] Som, T. and Karmakar, B. (2009). "Efficient green and red fluorescence upconversion in erbium doped new low phonon antimony glasses." *Optical Materials* 31, 609–618.

[19] Som, T. and Karmakar, B. (2010). "Surface plasmon resonance and enhanced fluorescence application of single-step synthesized elliptical nano gold embedded antimony glass dichroic nanocomposites." *Plasmonics* 5, 149-159.

[20] Som, T. and Karmakar, B. (2009). "Plasmon tuning of nano-Au in dichroic devitrified antimony glass nanocomposites by refractive index control." *Chemical Physics Letters* 479, 100–104.

[21] Som, T. and Karmakar, B. (2010). "Enhanced frequency upconversion of Sm^{3+} ions by elliptical Au nanoparticles in dichroic Sm^{3+}: Au-antimony glass nanocomposites." *Spectrochimica Acta Part A* 75, 640–646.

[22] Som, T. and Karmakar, B. (2009). "Enhancement of Er^{3+} upconverted luminescence in Er^{3+}: Au-antimony glass dichroic nanocomposites containing hexagonal Au nanoparticles" *Journal of the Optical Society of America B: Optical Physics* 26, B21-B27.

[23] Orman R. G. and Holland, D. (2007). "Thermal phase transitions in antimony (III) oxides." *Journal of Solid State Chemistry* 180, 2587-2596.

[24] Miller P. J. and Cody, C. A. (1982). "Infrared and raman investigation of vitreous antimony trioxide." *Spectrochimica Acta Part A: Molecular and Biomolecular Spectroscopy* 38, 555-559.

[25] Kamitsos, E. I., Patsis, A. P. and Chryssikos, G. D. (1993). "Infrared reflectance investigation of alkali borate glasses." *Journal of Non-Crystalline Solids* 152, 246-257.

[26] Motke, S. G., Yawale, S. P. and Yawale, S. S. (2005). "Infrared spectra of zinc doped lead borate glasses." *Bulletin of Materials Science* 25. 75-78.

[27] Scolze, H. (1991). *Glass Nature, Structure and Properties.* New York, Springer-Verlag, p. 145.

[28] Reddy, M. S., Raju, G. N., Nagarjuna, G. and Veeraiah, N. (2006). "Structural influence of aluminium, gallium and imdium metal oxides by means of dielectric and spectroscopic properties of CaO-Sb_2O_3-B_2O_3 glass system." *Journal of Alloys and Compounds* 464, 472-482.

[29] Reisfeld, R. (2005). *Nanostructured and Advanced Materials*. Vaseashta, et al. Eds., Springer, p. 77.

[30] Mott N. F. and Davis E. A. (1979). *Electronic processes in Non-Crystalline Materials.* 2nd Edition, Oxford, Clarendon Press.

[31] Karmakar, B. (2005). "IRRS, UV-Vis-NIR absorption and photoluminescence upconversion in Ho^{3+}-doped oxyfluorophosphate glasses." *Journal of Solid State Chemistry* 178, 2663-2672.

[32] Pauling, L. (1960). *The Nature of the Chemical Bond.* 3rd Edn., NewYork, Cornell University Press.

[33] Duffy, J. A. and Ingram, M. D. (1991). *Optical Properties of Glass.* Kreidl, N et al. Eds., Westerville, OH, American Ceramic Society.

[34] Duffy, J. A. and Ingram, M. D. (1992). "Comments on the application of optical basicity to glass". *Journal of Non-Crystalline Solids* 144, 76-80.

[35] Dimitrov, V. and Komatsu, T. (2002). "Classification of simple oxides: A polarizability approach" *Journal of Solid State Chemistry* 163, 100-112.

[36] Shackelford, J. F., Alexander, W. and Park J. S. (Eds.). (1994) *CRC Materials Science and Engineering Handbook*. Boca Raton, CRC Press, pp. S-14-21.

[37] Blech, I. A. (1986). *Properties of Materials in Electronics Engineering Handbook*. 2nd edition. Fink, D. G. and Christiansen D. Ed., New York, McGraw-Hill, pp. 6–30.

[38] de Araujo, R. E., de Araujo, C. B., Poirier, G., Poulain, M. and Messaddeq, Y. (2002). "Nonlinear optical absorption of antimony and lead oxyhalide glasses." *Applied Physics Letters* 81, 4694 – 4696.

[39] Dimitrov V. and Komatshu, T. (1999). "Electronic ion polarizabillity, optical basicity and metal (or nonmetal) binding energy of simple oxides." *Journal of the Ceramic Society of Japan* 107, 879-886.

[40] Biju, L P. R., Jose, G., Jyothy, P. V., Thomas, V. and Unnikrishnan, N. V. (2005). "Upconversion fluorescence in Sm^{3+} -doped zinc phosphate glassy matrix." *Journal of Modern Optics* 52, 2687-2694.

[41] Tripathi, G., Rai, V. K. and Rai, S. B. (2007). "Upconversion and temperature sensing behavior of Er^{3+} doped Bi_2O_3-Li_2O-BaO-PbO tertiary glass." *Optical Materials* 30, 201-206.

[42] Lin, H., Tanabe, S., Lin, L., Yang, D. L., Liu, K., Wong, W. H., Yu, J. Y. and Pun, E. Y. B. (2006). "Infrequent blue and green emission transitions from Eu^{3+} in heavy metal tellurite glasses with low phonon energy." *Physics Letter A* 358, 474-477.

[43] Xu, S., Fang, D., Zhang, Z. and Jiang, Z. (2005). "Effect of OH^- on the upconversion luminescence of Er^{3+}-doped oxyhalide tellurite glasses." *Journal of Solid State Chemistry* 178, 2159-2162

[44] Pisarski, W. A., Pisarska, J., Mączka, M. and Ryba-Romanowski, W. (2006). "Europium-doped lead fluoroborate glasses: Structural, thermal and optical investigations." *Journal of Molecular Structure* 792–793, 207-211.

[45] W.A. Weyl, Coloured Glasses, Society of Glass Technology, Sheffield, 1951.

[46] Doremus, R. H. (1964). "Optical properties of small gold particles." *The Journal of Chemical Physics* 40, 2389-2396.

[47] Eichelbaum, M., Rademann, K., Weigel, W., Löchel, B., Radtke, M. and Müller, R. (2007). "Gold-ruby glass in a new light: On the microstructuring of optical glasses with synchrotron radiation." *Gold Bulletin* 40(4), 278-282.

[48] Gonella F. (2007). "Metal nanocluster composite silicate glasses." Rev.Adv.Mater.Sci. 14, 134-143.

[49] de Lamaestre, R. E., Béa, H., Bernas, H., Belloni, J. and Marignier, J. L. (2007). "Irradiation-induced Ag nanocluster nucleation in silicate glasses: Analogy with photography." *Physical Review B* 76, 205431 [18 pages].

[50] Shin, J., Jang, K., Lim, K. –S., Sohn, I. –B., Noh, Y. –C. and Lee, J. (2008). "Formation and control of Au and Ag nanoparticles inside borate glasses using femtosecond laser and heat treatment" *Applied Physics A* 93, 923–927.

[51] Dubiel, M., Hofmeister, H. and Wendler, E. (2008). "Formation of nanoparticles in soda-lime glasses by single and double ion implantation." *Journal of Non-Crystalline Solids* 354, 607–611.

[52] Penninkhof, J. J., Polman, A., Sweatlock, L. A., Maier, S. A., Atwater, H. A., Vredenberg, A. M. and Kooi, B. J. (2003). "Mega-electron-volt ion beam induced anisotropic plasmon resonance of silver nanocrystals in glass." *Applied Physics Letters* 83, 4137-4139.

[53] Zhang, J., Dong, W., Sheng, J., Zheng, J., Li, J., Qiao, L. and Jiang, L. (2008). "Silver nanoclusters formation in ion-exchanges glasses by thermal annealing, UV-laser and X-ray irradiation." *Journal of Crystal Growth* 310, 234-239.

[54] Hofmeister, H., Drost, W. –G. and Berger, A. (1999). "Oriented prolate silver particles in glass-characteristics of novel dichroic polarizers." *Nanostructured Materials* 12 207-210.

[55] Podlipensky, A., Abdolvand, A., Seifert, G. and Graener, H. (2005). "Femtosecond laser assisted production of 3D structures in composite glass containing Ag nanoparticles." *Applied Physics A* 80, 1647-1652.

[56] Land, E. H. (1943). "Light polarizer and process of manufacture." *US Patent* 2,319,816.

[57] Fort, E., Ricolleau, C. and J. Sau-pueyo, (2003) "Dichroic thin films of silver nanoparticle chain arrays on facetted alumina templates." *Nano Letters* 3, 65-67.

[58] Kelly, K. L., Coronado, E., Zhao, L. L. and Schatz, G. C. (2003). "The optical properties of metal nanoparticles: The influence of size, shape, and dielectric environment." *The Journal of Physical Chemistry B* 107 (2003) 668-677.

[59] Dirix, Y., Bastiaansen, C., Caseri, W. and Smith, P. (1999). "Oriented pearl-necklace arrays of metallic nanoparticles in polymers: A new route toward polarization-dependent color filters." *Advanced Materials* 11, 223-227.

[60] Beall G. H. and Duke, D. A. (1983). *"Glass Ceramic Technology."* In: *Glass: Science and Technology.* Uhlman D. R. and Kreidl N. J. Eds., vol 1, San Diego, Academic Press.

[61] Mcmillan, P.W. (1979). *Glass–ceramics.*, London, Academic Press.

[62] Pardiñas-Blanco, I, Hoppe, C. E., López-Quintela, M.A. and Rivas, J. (2007). "Control on the dispersion of gold nanoparticles in an epoxy network." *Journal of Non-Crystalline Solids* 353, 826–828.

[63] Pérez-Juste, J., Pastoriza-Santos, I., M. Liz-Marzán, L., and Mulvaney, P. (2005). "Gold nanorods: Synthesis, characterization and applications." *Coordination Chemistry Reviews* 249, 1870–1901.

[64] Link S. and El-Sayed, M. A. (1999). "Spectral properties and relaxation dynamics of surface plasmon electronic oscillations in gold and silver nanodots and nanorods." *The Journal of Physical Chemistry B* 103, 8410-8426.

[65] De S. and De, G. (2008). In situ generation of Au nanoparticles in UV-curable refractive index controlled SiO_2-TiO_2-PEO hybrid films." *The Journal of Physical Chemistry C* 112, 10378–10384.

[66] Mulvaney, P. (1996). "Surface plasmon spectroscopy of nanosized metal particles." *Langmuir* 12, 788-800.

[67] Eichelbaum, M. and Rademann, K. (2009). "Plasmonic enhancement or energy transfer? On the luminescence of gold-, silver-, and lanthanide-doped silicate glasses and its potential for light-emitting devices, Adv. Funct. Mater. 19, 1–8.

[68] Zhang, J. Z. (2009). "Optical properties and spectroscopy of nanomaterials". Singapore, World Scientific Publishing Co. Pte. Ltd.

[69] Malta, O. L., Santa-Cruz, P. A., De Sá, G. F. and Auzel, F. (1985). "Fluorescence enhancement induced by the presence of small silver particles in Eu^{3+} doped materials." Journal of Luminescence 33, 261-272.

[70] Hayakawa, T., Selvan, S. T. and Nogami, M. (1999). "Field enhancement effect of small Ag particles on the fluorescence from Eu^{3+}-doped SiO_2 glass." *Applied Physics Letters* 74, 1513 (3 pp).

[71] Strohhöfer, C. and Polman, A. (2002). "Silver as a sensitizer for erbium." *Applied Physics Letters* 81, 1414 (3 pp).

[72] Mattarelli, M., Montagna, M., Vishnubhatla, K., Chiasera, A., Ferrari, M. and Righini, G. C. (2007). "Mechanisms of Ag to Er energy transfer in silicate glasses: A photoluminescence study." *Physical Review B* 75, 125102.

[73] Fukushima, M., Managaki, N., Fujii, M., Yanagi, H. and Hayashi, S. (2005). "Enhancement of 1.54-μm emission from Er-doped sol-gel SiO_2 films by Au-nanoparticles doping." Journal of Applied Physics 98, 24316 (4 pp.).

[74] Pan, Z., Ueda, A., Aga Jr., R., Burger, A., Mu, R. and Morgan, S.H. (2010). "Spectroscopic studies of Er^{3+} doped Ge-Ga-S glass containing silver nanoparticles." Journal of Non-Crystalline Solids 356, 1097-1101.

[75] de Almeida, R., da Silva, D. M., Kassab, L. R.P. and de Araújo, C. B. (2008). "Eu^{3+} luminescence in tellurite glasses with gold nanostructures." *Optics Communications* 281, 108–112.

[76] Kassab, L. R. P., da Silva, D. S., de Almeida, R. and de Araújo, C. B. (2009). "Photoluminescence enhancement by gold nanoparticles in Eu^{3+} doped GeO_2–Bi_2O_3 glasses." *Applied Physics Letters* 94, 101912.

[77] Jiménez, J. A., Lysenko, S., Liu, H., Fachini, E. and Cabrera, C. R. (2010). "Investigation of the influence of silver and tin on the luminescence of trivalent europium ions in glass." *Journal of Luminescence* 130, 163–167.

[78] Lide, D. R. Ed. (1975). *CRC Handbook of Chemistry and Physics.* 75th edn, Boca Raton, CRC Press, pp.8-21-34.

[79] Varnavski, O. P., Goodson, T., Mohamed, M. B. and El-Sayed, M. A. (2005). "Femtosecond excitation dynamics in gold nanospheres and nanorods." *Physical Review B* 72, 235405.